

# The Transient Ultra-luminous X-ray Source, ULX-4, in M51

S. Allak,<sup>1,2</sup>★ A. Akyuz,<sup>3,2</sup> İ. Akkaya Oralhan,<sup>4</sup> S. Avdan,<sup>2</sup> N. Aksaker,<sup>5,2</sup> A. Vinokurov,<sup>6</sup>  
F. Soyduğan,<sup>1,7</sup> E. Sonbas,<sup>8,9</sup> and K. S. Dhuga<sup>9</sup>

<sup>1</sup>Department of Physics, University of Çanakkale Onsekiz Mart, 17100, Çanakkale, Turkey

<sup>2</sup>Space Science and Solar Energy Research and Application Center (UZAYMER), University of Çukurova, 01330, Adana, Turkey

<sup>3</sup>Department of Physics, University of Çukurova, 01330, Adana, Turkey

<sup>4</sup>Department of Astronomy and Space Sciences, Erciyes University, 38039, Kayseri, Turkey

<sup>5</sup>Adana Organised Industrial Zones Vocational School of Technical Science, University of Çukurova, 01410, Adana, Turkey

<sup>6</sup>Special Astrophysical Observatory of the Russian AS, Nizhnij Arkhyz, Russia

<sup>7</sup>Astrophysics Research Centre and Ulupinar Observatory, University of Çanakkale Onsekiz Mart, 17100, Çanakkale, Turkey

<sup>8</sup>Adiyaman University, Department of Physics, 02040 Adiyaman, Turkey

<sup>9</sup>Department of Physics, The George Washington University, Washington, DC 20052, USA

Accepted 2021 December 14. Received 2021 December 2; in original form 2021 June 14.

## ABSTRACT

We present the results of a temporal and spectral analysis of the transient source ULX-4 in the galaxy M51. The data used were drawn from *Chandra*, *XMM-Newton* and *Swift-XRT* archives, spanning the years 2000–2019. The X-ray flux of the source is seen to vary by two orders of magnitudes within a month but a short-term variability was not observed over the time intervals of 100–2000 second in the 0.3–10 keV energy band. We find some evidence for the existence of bi-modality feature in the flux distribution of ULX-4. We identified two optical sources as possible counterparts within an error radius of 0.''18 at 95% confidence level for ULX-4 based on the archival *HST*/ACS and *HST*/WFC3 data. Blackbody fits of the spectral energy distributions (SEDs) indicate the spectral type to be B-type stars. One of these counterparts exhibits a low-amplitude optical periodicity of  $264 \pm 37$  days in the F606W filter; if we assume this apparent periodicity is associated with the orbital motion of the donor, then it is more likely that the donor is a red supergiant satisfying the long periodicity and accretion via Roche-lobe overflow. Consequently, the SED would then have to be interpreted as a superposition of emissions from a cold donor and a hot flow component, most likely from an accretion disk. If, on the other hand, the periodicity is super orbital in nature i.e., due to possible interactions of the compact object with a circumstellar disk, the donor could then be a Be/X star hosting a neutron star.

**Key words:** galaxies: individual (M51) X-rays: binaries–X-rays: general

## 1 INTRODUCTION

Ultraluminous X-ray Sources (ULXs) are point-like sources in external galaxies with an X-ray luminosity ( $L_X \geq 10^{39}$  erg s<sup>−1</sup>) exceeding the Eddington limit for a stellar-mass black hole. They are not located in the center of their host galaxies. This rules out the possibility of them being a supermassive black hole as a source of high emission (e.g. Kaaret et al. 2017; Fabrika et al. 2021, for a review). Recent studies tend to lean toward the majority of ULXs hosting stellar mass compact objects undergoing super-Eddington (Fürst et al. 2017; Ghosh & Rana 2021) rather than sub-Eddington

accretions onto intermediate mass black holes (IMBHs) (Colbert & Mushotzky 1999; Titarchuk & Seifina 2016; Mezcua 2017). In the case of super-Eddington accretion, the possible compact objects in ULXs may be either black holes (BHs) or neutron stars (NSs). While their relative numbers are still quite uncertain, the ULXs harboring NSs could be significantly more numerous than observed (Wiktorowicz et al. 2017; King & Lasota 2020). So far, the presence of NSs in six ULXs has been confirmed by pulse detections and are known as pulsating ULXs (PULXs): M82 X2 (Bachetti et al. 2014), NGC 7793 P13 (Fürst et al. 2016; Israel et al. 2017b), NGC 5907 ULX-1 (Israel et al. 2017a,b), NGC 300 ULX-1 (Carpano et al. 2018), NGC 1313 X-2 (Sathyaprakash et al. 2019), M51 ULX-7 (Rodríguez Castillo et al. 2020). In addition,

★ E-mail: 0417allaksinan@gmail.com

Brightman et al. (2018) discovered that M51 ULX-8 has a cyclotron resonance scattering feature. This feature is presumably caused by the interactions of charged particles with a strong magnetic field, thus suggesting that ULX-8 hosts a NS. Also the first Galactic PULX (Swift J0243.6+6124) was discovered by the Swift/XRT telescope and X-ray pulsations at  $\sim 9.86$  s were detected in the 0.2–10 keV band (Kennea et al. 2017). Detected pulsations were then confirmed by data from different X-ray observatories (Beardmore et al. 2017; Bahramian et al. 2017; Jaisawal et al. 2018; Beri et al. 2021) and Fermi Gamma-Ray Burst Monitor (GBM) (Jenke & Wilson-Hodge 2017).

It is known that ULXs are variable sources and their flux values in star-forming galaxies can vary by an order of magnitude (Feng & Kaaret 2009). However, a small fraction of ULXs for which flux variation reaches up to two orders of magnitude, are in the transient source class. Thanks to the new generation of X-ray observatories, the number of observations of these sources is rapidly increasing. This is likely to increase the discovery of new transient sources as well (e.g. Middleton et al. 2012; Barnard et al. 2013; Hu et al. 2018; van Haften et al. 2019; Allak et al. 2020; Walton et al. 2021). PULXs are sources observed in this class with their high flux variability reaching up to factors of 50 in flux variation (e.g. Fürst et al. 2017; Pintore et al. 2020). This high variation has been interpreted in terms of the onset of a propeller mechanism (Tsygankov et al. 2016) and/or a super-orbital effect (Brightman et al. 2019).

Investigation of ULXs in the optical wavelengths as well as the X-ray band can help reveal their physical nature. In particular, identification and characterization of the optical counterparts of ULXs plays an important role in advancing our understanding of the origin of the emission, whether it is primarily from the accretion disk and/or the donor star. Unfortunately, unique identification of the optical counterparts is not straightforward since most of them are located in very crowded regions or even in/near star clusters. Also, most optical counterparts are too faint (apparent magnitudes  $m_V > 21$  mag) to be detected by ground-based observations (Tao et al. 2011; Gladstone et al. 2013; Vinokurov et al. 2018). However, there are few exceptions with  $m_V \sim 20$  mag or even brighter, for example, NGC 7793 P13 (Motch et al. 2014), NGC 300 ULX-1/SN2010da (Villar et al. 2016) and UGC 6456 ULX (Vinokurov et al. 2020). The absolute magnitudes ( $M_V$ ) of ULXs are in the range of  $-3 < M_V < -8$  mag (Vinokurov et al. 2018). There are hundreds of ULXs but only about 20 have a single optical counterpart (Tao et al. 2011; Gladstone et al. 2013; Avdan et al. 2019; Allak et al. 2020). Multiple optical counterparts have been detected for a number of ULXs (Soria et al. 2005; Mucciarelli et al. 2007; Avdan et al. 2019; Aksaker et al. 2019; Akyuz et al. 2020).

The galaxy M51 (NGC 5194), also known as the Whirlpool galaxy, and its companion NGC 5195 are a pair of interacting galaxies located within the constellation Canes Venatici. The face-on spiral galaxy M51 has a low luminosity Seyfert 2 nucleus (at a distance of 9 Mpc; Rodríguez et al. (2014); Song et al. (2020)). The remarkable aspect of the spiral arms of M51 is that they are very symmetric and serve as star formation factories as a result of the continuous and extremely regular dust lanes and the presence of diffuse interstellar medium (Block et al. 1997). As such, M51 is a good target for studying discrete X-ray populations, including ULXs.

X-ray sources in M51 were investigated using the ROSAT/HRI observations. Among the nine X-ray sources detected, only three of them have luminosities of  $L_X > 10^{39}$  erg s $^{-1}$  (Roberts & Warwick 2000; Colbert & Ptak 2002).

Also 113 X-ray sources within the optical extents of the galaxy pair (NGC 5194/5195) were detected by Terashima & Wilson (2004) using the 2000 and 2001 *Chandra* ACIS-S observations. Seven of these sources have  $L_X > 10^{39}$  erg s $^{-1}$  in the 0.5–8 keV range. Later, Dewangan et al. (2005) confirmed these seven ULXs and detected a new one using an *XMM-Newton* EPIC observation. They examined both short and long-term variability of the sources in detail.

Urquhart & Soria (2016) presented the discovery of X-ray eclipses in two ULXs, ULX-1 and ULX-2 located in the same region of M51, by analyzing archival *Chandra* and *XMM-Newton* data. They reported the binary period of ULX-1 was constrained to be either  $\approx 6.3$  days, or  $\approx 12.5$ –13 days. Also, Urquhart et al. (2018) investigated the optical properties of these ULXs using *HST*, *LBT* and *VLA* observations and they determined that both ULXs were associated with ionized nebulae. Rodríguez Castillo et al. (2020) discovered 2.8 s pulsations in the X-ray emission of the M51 ULX-7 using *XMM-Newton* data. The variable source ULX-7 has  $L_X$  between  $10^{39}$  and  $10^{40}$  erg s $^{-1}$  and a dipole field component in the range of  $10^{12}$  G  $\leq B_{dipole} \leq 10^{13}$  G was suggested considering the observed luminosity. They reported the presence of a sinusoidal pulse shape with large variations in amplitude. According to their findings the system contains a massive OB giant or supergiant donor. In addition, Brightman et al. (2020) found that ULX-7 has a super-orbital period as 38 days. Moreover, they identified a new transient ULX, XT-1, reaching a peak luminosity of  $10^{40}$  erg s $^{-1}$ .

The M51 galaxy hosts a large number of transient X-ray sources: One of them is the well-known source ULX-4. The first detection of ULX-4 was reported by Terashima & Wilson (2004). They presented that the flux value of ULX-4 (source 37, in their Table 2) increased by two orders of magnitude within the energy range (0.5–8 keV) from the analysis of 2000 and 2001 *Chandra* data. Also, ULX-4 is one of 8 ULXs catalogued by Swartz et al. (2011) in this galaxy pair, and its unabsorbed luminosity is  $L_X = 2.2 \times 10^{39}$  erg s $^{-1}$  in the (0.3–10) keV energy range. Recently, Earnshaw et al. (2018), Song et al. (2020) and Brightman et al. (2020) reported the long-term flux variability of some of the ULXs in M51 including ULX-4 using *XMM-Newton*, *Chandra* and *Swift-XRT* observations.

In the present work, we focus on determining the nature of the transient source ULX-4 and its potential optical counterpart. Toward these goals, we carried out comprehensive spectral and temporal analyses of the X-ray observations of ULX-4 using the archival *XMM-Newton*, *Chandra* and *Swift* observations. A number of these observations have not been used in previous studies of this source. In addition, we make extensive use of archival *HST* observations in an effort to isolate and identify possible optical counterparts of ULX-4.

The paper is organized as follows: Section 2 contains information on the X-ray and optical observations together with the details of the data reduction, along with the methodology deployed in the analysis of these data. In Section 3, we present and discuss the main results. Finally, in Section 4, we conclude by summarizing our major findings.

## 2 OBSERVATIONS, DATA REDUCTION AND ANALYSIS

### 2.1 X-Ray Data

The source (ULX-4) was observed multiple times with *XMM-Newton*, *Chandra* and *Swift-XRT* over 20 years. Log of *XMM-Newton* and *Chandra* observations used are given in Table 1. The true color images of the source from the *XMM-Newton*, *Chandra* and *Swift-XRT* are shown in Fig. 1.

M51 ULX-4 was observed by *Swift-XRT* multiple times (276 observations) between 2005 and 2021. The target IDs of the observations we used in this study are 10717, 11417, 32017, 37267, 81964, 11106, 30083, 35895, 80113 and 745090. These observations have very different exposures. For example, the minimum exposure time is 5 s and maximum exposure time is 6857.3 s. Mostly the exposure times of the observations are around 1500 s.

The *XMM-Newton* EPIC data were analyzed with Science Analysis System (sas)<sup>1</sup> v17.0 software. The *epchain* and *emchain* tasks were used to obtain EPIC-pn and MOS event files for each observation. The events corresponding to PATTERN $\leq$ 12 and PATTERN $\leq$ 4 with FLAG=0 were selected for EPIC-MOS and pn cameras, respectively. We followed the standard procedure of extracting the source and the background events by deploying a circular radius of 15'' with the *evselect* task. We note though that if we compare *XMM-Newton* and *Chandra* images, it is clear that in most of the *Chandra* observations, that a number of faint point sources are located near ULX-4 and fall within the radius of 15'' region. This invariably contaminates the source counts for ULX-4.

*Chandra* ACIS-S and ACIS-I observations were analyzed by using Chandra Interactive Analysis of Observations (CIAO)<sup>2</sup> v4.12 software and calibration files CALDB v4.9. The level 2 event files were obtained with *chandra\_repro* in CIAO. The source and the background events were extracted from circular regions of 5'' radius. We obtained the source spectra and light curves with the tasks *specextract* and *dmextract*, respectively.

The count rates for *Swift-XRT* in PC mode were extracted using automated procedures (Evans et al. 2009) specified on the web page<sup>3</sup>. In PC mode, source counts were extracted from a radius of 30 pixel circular region centered on the source position. The background counts were extracted from an annulus centered on the source with inner and outer radii of 60 pixels (142'') and 110 pixels (260''), respectively. As noted in the study of (Evans et al. 2009), some sources falling into the background region are excluded from the background estimate. We chose the default value of 20 counts/bin which the minimum number of counts a bin must contain to be considered complete in compliance with the guidelines indicated on the aforementioned website. When we applied these procedures, we used 82 observations with total counts greater than zero in the 0.3-10 keV energy band. ULX-4 has been observed four times with *NuSTAR* between 2017 and 2019. However, the source was not spatially resolved in these observations.

### 2.1.1 Spectral Fitting

The spectral properties of ULX-4 have been studied by several authors using *XMM-Newton* and *Chandra* data (e.g. Dewangan et al. 2005; Terashima et al. 2006). In this study, C13, C14, XM6, XM7, XM8 data sets were used for the first time for spectral analysis. In addition, the data sets used in previous studies were reanalyzed in detail. The ULX-4 spectra with the instrument responses and ancillary files were generated for *XMM-Newton*, *Chandra* and *Swift-XRT* observations. The spectral fitting was performed with *XSPEC* v12.8.2 for each observation. According to the total source counts, the source energy spectra were grouped with the FTOOLS *grppha* at least 10 and 30 counts per energy bin for *Chandra* and *XMM-Newton* data, respectively.

As discussed in several studies, one-component models should be considered statistically when the data quality is low and exposure is short. However, these models tend not to provide sufficiently accurate descriptions of the ULX spectra and hence the interpretation of the physical origin of the spectra remains questionable (Gladstone et al. 2009; Sutton et al. 2013; Kaaret et al. 2017). Although we do not have high quality data, we investigated single and two component models which are widely adopted in the literature (Gladstone et al. 2009; Koliopanos et al. 2017; Earnshaw et al. 2020a; Walton et al. 2021). The ULX-4 spectra were fitted with single component models such as a *power-law*, *diskblackbody* (*diskbb*), *pfree diskblackbody* (*diskpbb*), broken power-law (*bkn-power*) and Comptonization (*compTT*) model. We did attempt two component models such as *power-law+diskbb*, *power-law+mekal*, *power-law+diskpbb*, *diskbb+compTT* and *diskbb+cutoffpl*. In addition to these models, we included two absorption components (*tbabs*). One of the absorption models represented the line-of-sight column density, which we kept fixed at the Galactic value  $N_H = 3 \times 10^{20} \text{ cm}^{-2}$  (Dickey & Lockman 1990) and the other was left free to account for intrinsic absorption. We found that the intrinsic absorption values are small enough (between  $10^{13} - 10^{17} \text{ cm}^{-2}$ ) to be negligible for all observations. Therefore, a fixed column density (Galactic  $N_H$ ) was used throughout this work.

In spectral analyses of the *XMM-Newton* and *Chandra* data, the spectral fits obtained show a wide range of  $\chi^2_\nu$  values, therefore, the single and two component models were examined according to the  $\chi^2_\nu$  values in the range of  $0.8 < \chi^2_\nu < 2$  and F-test results. The *power-law* model fits are statistically better than the other single component models at a  $3\sigma$  confidence level for the *XMM-Newton* and *Chandra* datasets. On the other hand, using two-component models, no statistically significant improvement was achieved in fitting of the datasets, except for XM1 data. Only the spectrum of XM1 gives better statistics according to the F-test for the *power-law+mekal* model at  $3\sigma$ , along with well constrained model parameters and  $\chi^2_\nu$  statistics. Also, for the majority of the datasets, the parameters of the two-component models do not appear to be well constrained, although they have statistically acceptable fits in terms of reduced  $\chi^2_\nu$  interval.

The values given in Table 2 show the best model parameters. With the exception of the XM1 dataset, the parameters of the two-component models for the majority of the other datasets are unlikely to be meaningful considering the large uncertainties although the  $\chi^2_\nu$  are in the range of 0.8 to 2, a range on the border of being acceptable.

The unabsorbed fluxes of ULX-4 were calculated in the energy band 0.3–10 keV using the convolution model *CFLUX* available in *XSPEC* and the source luminosity values were calculated assuming a distance of 9 Mpc. The *power-law* model does not have a natural cut-off at low energies, therefore the unabsorbed source fluxes can be overestimated. Considering this, we calculated the absorbed fluxes for observations with sufficient data statistics using the power law model. However, we found that there are negligible differences between the absorbed and unabsorbed flux values for all datasets. Therefore, only the unabsorbed fluxes are listed in Table 2.

In Table 2, the well-fitted spectral model parameters for ULX-4 obtained with *XMM-Newton* and *Chandra* data are given with unabsorbed flux values. Three (XM6, XM7 and XM8) out of eight *XMM-Newton* observations we used do not have EPIC-MOS data. There appears to be too much noise in the MOS data for the majority of datasets, therefore, simultaneous fits of EPIC pn + MOS spectra do not produce acceptable model parameters and their chi-square statistics do not improve (except for XM1).

<sup>1</sup> <https://www.cosmos.esa.int/web/xmm-newton/sas>

<sup>2</sup> <https://xc.harvard.edu/ciao/>

<sup>3</sup> [https://www.swift.ac.uk/user\\_objects/](https://www.swift.ac.uk/user_objects/)



### 2.1.2 Short-term X-ray Variability

We searched for short-term variability of ULX-4 with recently available data of XM6, XM7, XM8, C13 and C14. The background subtracted X-ray light curves of ULX-4 were binned over intervals of 100s, 500s, 1000s and 2000s in the 0.3–10 keV energy band using *evselect* in *SAS*. The resulting light curves were tested for short-term count variations using  $\chi^2_\nu$  test. This test was applied to search for large amplitude variations with respect to the constant count rate hypothesis. The results of  $\chi^2$  test were examined together with the probability values  $P(\text{var})$ , an indicator of the variability of data. If  $P(\text{var})$  exceeds 95% taken as the limit, it could be interpreted as data variability. However, we found a  $P(\text{var})$  value of  $\sim 57\%$ . This moderate value suggests that ULX-4 does not show any significant amplitude variation.

In addition, the background subtracted X-ray light curves, sampled at 0.1 s, yielding 5 Hz Nyquist frequency, were Fourier transformed to generate power density spectra (PDS) using the utility *XRONOS* v6.0 in *HEASOFT* v6.27. Initially, the entire duration of the light curves was included in the transform to look for overall variability features but none were found. Then, the total exposure was divided into eight time intervals, and the (transform) procedure was repeated. No signal stronger than  $1.5\sigma$  significance was detected.

### 2.1.3 Long-term X-ray Variability

We also probed the long-term variability of ULX-4 by deploying the more recent data adding to previous studies of [Earnshaw et al. \(2018\)](#), [Song et al. \(2020\)](#), and [Brightman et al. \(2020\)](#). The background subtracted source count rates for *XMM-Newton* and *Chandra* data were obtained for the light curve in 0.3–10 keV energy band using *XSPEC*. The background subtracted source count rates of *Swift-XRT* in PC mode were extracted using standard procedures. We only used 82 data sets, between 2005–2021 years, from which the source was detected or  $3\sigma$  upper limits could be obtained. All these count rates were converted to fluxes with the best fitting parameters of *power-law* model  $\Gamma = 1.75$  and  $N_H = 3 \times 10^{20} \text{ cm}^{-2}$  using the *WebPIMMS* tool<sup>4</sup>. In addition, the count rates for C1 and C3 data sets were obtained by using *srcflux* tool in *CIAO* with the same  $\Gamma$  and  $N_H$  for  $3\sigma$  upper limit. The resultant long-term light curve of ULX-4 is given in Fig. 2. The *XMM-Newton* and *Swift-XRT* detectors do not have sufficient spatial resolution to resolve sources too close to ULX-4. Although we chose a small source extraction region (radius of  $15''$ ) for *XMM-Newton* data, there are still three faint transient X-ray sources detected within this region. To calculate the contributions of these three sources, we derived their fluxes using all *Chandra* observations given in Table 1. For this, *CIAO*'s *srcflux* task was used by taking the photon index of  $\Gamma=1.7$  and  $N_H=0.03 \times 10^{22}$ . We calculated the maximum total flux from the contaminants as  $2.29 \times 10^{-14} \text{ erg cm}^{-2} \text{ s}^{-1}$ . This potentially implies that the *XMM-Newton* and *Swift-XRT* fluxes of ULX-4 are overestimated by this amount due to the presence of these nearby sources. However, we need to keep in mind that these sources are transient and the observations are not simultaneous.

We constructed Lomb-Scargle (LS) periodograms ([Lomb 1976](#); [Scargle 1982](#)) to search for periodic modulations of the ULX-4 system for the long-term light curve by using a *Python*<sup>5</sup> subroutine. However, no periodicity was detected in the period range 2–3000

days from any of the X-ray data. In addition, we re-ran the LS analysis on subsets of close observations. For this, we divided the light curve into six epochs. These epochs were defined as Epoch 1: 2005, Epoch 2: 2007, Epoch 3: 2011, Epoch 4: 2012, Epoch 5: 2018–2021, Epoch 6: 2011+2012. However, we did not find any significant periodicity for these epochs.

### 2.1.4 Time Lags

Evidence for the presence of spectral lags (both hard and soft) in a number of variable ULXs including NGC 5408 X-1 ([Heil & Vaughan 2010](#); [De Marco et al. 2013](#); [Hernández-García et al. 2015](#)), NGC 55 ULX-1 ([Pinto et al. 2017](#)), NGC 1313 X-1 ([Kara et al. 2020](#)), and NGC 4559 X-1 ([Pintore et al. 2021](#)) has been reported. These lags are thought to involve the accretion flow and strong outflow winds in which the hard photons propagate through an extended optically thick medium, the origin of which is speculated to be the base of the outflows. Another possible scenario, proposed by [de Avellar et al. \(2013\)](#) for hard lags, is that it represents the light-travel time between the corona and/or the neutron star surface or boundary layer, and the innermost region of the accretion disc. In X-ray binaries hard lags are usually seen for the upper kHz QPOs for which the frequency of either the lower or the upper kHz QPO is equal to the Keplerian frequency at the inner edge of the accretion disc (e.g. [Miller et al. \(1998\)](#); [Osherovich & Titarchuk \(1999\)](#); [Stella & Vietri \(1999\)](#)). As ULX-4 indicates a relatively high degree of variability based on the hardness-intensity diagram, we have attempted an extraction of frequency-dependent time lags following the procedure outlined in [Uttley et al. \(2014\)](#) and [Pintore et al. \(2021\)](#). We used background subtracted *Chandra* (C2, C4, C11, C12, C14) light curves in the 0.3–2 keV and 2–10 keV energy bands for which the source counting statistics are comparable. We also extracted lags for the following bands: 0.3 – 1.0 keV and 1.0 – 7.0 keV. We performed FFT for the full range of the two light curves binned with  $\Delta T=100$  s over 3 to 15 intervals depending on the duration of the light curve (with each segment being 5 ks in duration). The resulting power spectra were averaged and then cross-correlated to obtain the spectral lag as a function of frequency ([Huppenkothen et al. 2019a,b](#)). We summarize our results as follows: the weighted spectral lags are consistent with zero within error bars for both sets of the energy bands. We note, in passing, that if we follow the procedure of [Pintore et al. \(2021\)](#) i.e., taking the average lag over a certain narrow frequency range, for which the coherence is relatively high, we too find a hard lag for one of the light curves (C2); the value is moderately high ( $758 \pm 317$  s) but is quite sensitive to the chosen frequency range ( $2.0\text{E-4} - 4.4\text{E-4}$ ) and the average coherence level (0.33).

In order to assess the statistical significance of the extracted time lag, we performed a Monte Carlo simulation of 1000 light curves and extracted frequency-resolved lags and the associated coherence. The simulations were setup with the mean count-rate and rms variability parameters estimated from the *Chandra* light curves for the 0.3–2.0 keV and 2.0 – 10 keV bands. We used the broken-power law (BPL) as the spectral model with nominal parameters. The resulting light curves (25 ks in duration and binned at 100 seconds) were analyzed and frequency-resolved time lags were extracted using the *STINGRAY* package following the procedure outlined in [Uttley et al. \(2014\)](#) and [Pintore et al. \(2021\)](#). We found the mean time lags and the coherence to be consistent with zero within the uncertainties. As another check, we also averaged the mean lags over a narrow frequency range (i.e.,  $(2-4.4) \times 10^{-4}$  Hz)

<sup>4</sup> <https://heasarc.gsfc.nasa.gov/cgi-bin/Tools/w3pimms/w3pimms.pl>

<sup>5</sup> <https://docs.astropy.org/en/stable/timeseries/lombscargle.html>



for a number of individual light curve combinations for which the coherence was found to be in range  $\geq 0.4$  and above. We obtained the average to be  $349 \pm 189$  s for one of the light curve combinations. In totality, approximately 60 light curve-combinations from our sample of 1000 light curves (over two energy channels each) yield a similar result thus suggesting that a marginally significant lag can be obtained spuriously (with a relatively high probability of  $\sim 6\%$ ) over a limited frequency range. We thus urge caution in attaching a physical significance to the experimentally extracted lag noted above.

### 2.1.5 New Transient X-ray Source: CXOU J132951.7+471010

In the process of analyzing the *Chandra* observations from 2017, we identified a new transient source. As shown in Fig.3, this transient source, shown in panel C13 as a white dash circle, is not seen in the other available *XMM-Newton* and *Chandra* observations. We determined that the source is located at the coordinates R.A (J2000) =  $13^{\text{h}}29^{\text{m}}51^{\text{s}}.7$ , Dec. (J2000) =  $+47^{\circ}10'10.''10$  (see Fig.3) using CIAO *wavdetect* tool and it has not been cataloged by Kuntz et al. (2016). In addition, we were unable to find this source in the Transient Name Server<sup>6</sup> among the transients in M51. For convenience we use the acronym CXOU (for *Chandra* X-ray Observatory Unregistered source) and name this source as CXOU J132951.7+471010. Its count rate is found as  $(9 \pm 3.12) \times 10^{-4}$  count/s in the 0.3–10 keV energy range from 2017 *Chandra* data. Flux upper-limits for non-detections were also derived at  $3\sigma$  assuming a power-law spectrum with  $\Gamma = 1.7$  and  $N_H = 3 \times 10^{20} \text{ cm}^{-2}$  using SRCFLUX tool in CIAO. *Chandra* flux was obtained with help of WebPIMMS tool by using the same parameters. We obtained the unabsorbed flux of CXOU J132951.7+471010 in the range of  $(0.05\text{--}1.88) \times 10^{-14} \text{ erg cm}^{-2} \text{ s}^{-1}$  and the corresponding luminosity of  $(0.05\text{--}2) \times 10^{38} \text{ erg s}^{-1}$  assuming a distance of 9 Mpc.

## 2.2 Optical Data

### 2.2.1 Astrometry

We used *HST* archival data (see Table 3 for details) to investigate the optical properties of ULX-4. For a relative astrometry between *Chandra* (ObsID 13816) and *HST* (ObsID J97C51R4Q) images, we followed a similar method that we used in our previous works (Allak et al. 2020; Ozdogan Ela et al. 2021). The DAOFIND tool in IRAF<sup>7</sup> and *wavdetect* tool in CIAO were used for source detection in *HST* and *Chandra* images, respectively. In both images, three isolated and point reference sources were matched; their coordinates and counts are given in Table 4. These reference sources are (1) the SN 2011dh (Hosh et al. 2013), (2) an X-ray binary (CXOU J133006.5+470834) (Kuntz et al. 2016) and (3) a background radio source (J133011+471041) (Rampadarath et al. 2015). We derived the offsets between these *Chandra* and *HST* reference sources as  $0.''21$ ,  $0.''17$  and  $0.''18$ , respectively at 90% confidence level. The astrometric errors between the *Chandra* and *HST* images were found  $0.''14$  for R.A. and  $0.''11$  for Dec. The astrometric correction was calculated using quadratic sum for the standard deviations of these errors. As a result, we found the position of the ULX-4 on the *HST* image within an error radius of  $0.''18$  at 95% confidence level. We identified two optical counterparts within the error radius and

labelled them as A and B according to their increasing Dec. The corrected coordinates of ULX-4 are also given in Table 4. The *HST* three color (red, green and blue; RGB) image showing the position of ULX-4 and its optical counterparts (A and B) is depicted in Fig.4.

### 2.2.2 Photometry

Point Spread Function (PSF) photometry was performed to determine the magnitudes of optical sources using the DAOPHOT package (Stetson 1987) in IRAF. In order to obtain photometric errors, we multiplied the pixel values by the exposure time using IMARITH tool to calculate the electron/pixel. Thirty bright and isolated sources near the optical counterparts for ULX-4 were selected to build the PSF model. PSF fitting radius was taken as 3 pixels in the *all-star* task. For ACS/WFC and WFC3 filters, the zero-points were obtained from PYSYNPHOT<sup>8</sup> which are given in Table 5. We performed aperture corrections with a radius between  $0.''05$  to  $0.''5$  for ACS/WFC and ACS/WFC3.

### 2.2.3 Spectral Observations

The obtained magnitudes of the optical counterparts were corrected for extinction using the ratios of Balmer lines of the region of ULX-4. For this purpose, spectral data were obtained from the TUG Faint-Object Spectrograph and Camera (TFOSC) instrument mounted on RTT150 (Russian–Turkish Telescope in Antalya, Turkey)<sup>9</sup> on 16 July 2018. The derived  $H_\alpha$  and  $H_\beta$  flux ratio for the spectrum have been taken into account to determine Balmer decrements. The standard data reduction steps were performed using IRAF. For the reddening calculation, intrinsic Balmer decrements ratio  $(H_\alpha/H_\beta)_{\text{int}}$  value was taken as the standard 2.87 for star forming galaxies, estimated using the temperature  $T = 10^4 \text{ K}$  and electron density  $n_e = 10^2 \text{ cm}^{-3}$  for Case B of Osterbrock (1989).  $E(B-V)$  was found as 0.15 mag. from the ratio of hydrogen Balmer lines. Then,  $A_V$  was calculated as 0.46 mag using the equation of  $A_V = R_V \times E(B-V)$ , where the extinction factor of  $R_V$  is 3.1 (Cardelli & Wallerstein 1989). The extinction corrected magnitudes of the optical counterparts were calculated in accordance with  $A_V$  given in Table 5.

Also we found a single optical counterpart of the CXOU J132951.7+471010 source within the error radius of  $0.''27$  at 99.7% confidence level. The optical counterpart of CXOU J132951.7+471010 is detected only in UV bands ( $m_{F275W} 22.03 \pm 0.04$  mag and  $m_{F336W} 22.88 \pm 0.03$  mag).

### 2.2.4 Spectral Energy Distribution

Assuming optical emission originates from the donor star, the spectral types of optical counterparts were estimated from Spectral Energy Distributions (SEDs) obtained by using PYSYNPHOT. The CK04 standard stellar spectra templates were used in this program (Castelli & Kurucz 2004). The flux values of the counterparts of A and B were obtained from the magnitudes given in Table 5. All synthetic spectra were derived with metallicity of  $Z = 0.015$  (Urquhart et al. 2018) and extinction of  $A_V = 0.46$  mag. Also, synthetic spectra were normalized with Vega  $m_V = 0$  mag. In SED plots, the wavelength of the filters were selected as the pivot wavelength, obtained from PYSYNPHOT. By way of a comparison of the spectral features of the optical counterparts, with those of two field stars (R1 and R2 in

<sup>6</sup> <https://wis-tns.weizmann.ac.il>

<sup>7</sup> <http://ast.noao.edu/data/software>

<sup>8</sup> <https://pysynphot.readthedocs.io/en/latest/>

<sup>9</sup> <http://tug.tubitak.gov.tr/en/teleskoplar/rtt150-telescope-0>

Fig.4), the SEDs of optical counterparts and selected field stars are shown in Fig.5.

In addition, as an alternative way to determine the spectral type of counterparts, we fitted a blackbody model to the SEDs of these counterparts. A code has been used with `OPTIMSET` and `FMINSEARCH` functions in `MATLAB`<sup>10</sup> to get a blackbody spectrum. The SEDs for the optical counterparts A and B are adequately fitted to a blackbody spectrum with temperatures of  $26554 \pm 104$  K and  $21386 \pm 173$  K, respectively, at 95% confidence level. The  $\chi^2_\nu$  values were found 0.88 and 0.91, respectively. The number of degrees of freedom is four. Moreover, R1 and R2 are also well-fitted to a black-body spectrum with temperatures of  $27200 \pm 187$  K and  $17378 \pm 214$  K, respectively, at 95% confidence level.

### 2.2.5 Long-term Optical Variability

In order to search for periodic modulations, we constructed long-term light curves. We used thirty *HST* ACS/WFC F606W and F814W observations (Proposal ID: 14704) with the same exposure time of 2200 s. The same procedure (as given in Section 2.2.2) was followed for PSF photometry for all observations.

A moderate periodic modulation was determined for counterpart A in the F606W filter. No modulation was observed in the F814W filter. For counterpart B, no modulation with significant amplitude was found in either filter. To check whether the modulation in counterpart A could be due to systematic error, we obtained the light curves of 10 reference sources. These reference sources were selected as bright sources close to counterpart A within the white circle in Fig.4. We did not find any periodic modulation in the reference sources. Then we calculated the average magnitude of the source using the magnitudes of 30 observations. We calculated the deviations of magnitude by taking the difference of the source's average magnitude from its magnitude value. Afterwards, these deviations were subtracted from the magnitude of counterpart A for each observation which are given in Table 6. As a result, a periodic modulation was seen clearly from the corrected light curve of the counterpart A in the F606W images (Fig.7). We fitted a sinusoidal curve using the equation  $m(t) = \bar{m} + A \sin[2\pi(t-t_1)/P + \phi]$  given by Liu et al. (2009). Here,  $P$  is a period,  $\phi$  is a phase angle,  $t$  is the reference time,  $A$  is amplitude and  $\bar{m}$  is an average magnitude. When we applied this sinusoidal fit to the light curve,  $P = 264.45 \pm 36.81$  days,  $A = 0.07 \pm 0.02$  magnitude and  $\phi = 96^\circ.35 \pm 0.78$ . These values were obtained with  $\chi^2/\text{dof} = 21.06/27$  at 99.7% confidence level.

### 2.2.6 Age and Mass Estimation of a Nearby Cluster

It is known that the bright X-ray sources are located near star clusters and their physical parameters such as mass and age provide information about their nature (Zezas & Fabbiano 2002). In our study, optical counterparts of ULX-4 are also located near a star cluster with coordinates of R.A. =  $13^{\text{h}}29^{\text{m}}53^{\text{s}}.278$  and Dec. =  $+47^\circ 10' 42''.55$  cataloged by Chandar et al. (2016). In Fig.4, the location of the cluster and optical counterparts are shown. We derived the age and mass values of this cluster using the data obtained from ACS/WFC and ACS/WFC3 (see Table 3). For this calculation, we performed aperture photometry with the radius of  $0.''4$  using *apphot* package in *IRAF*. We obtained magnitudes for F336W, F435W, F555W and

F814W filters as  $17.92 \pm 0.01$  mag,  $19.04 \pm 0.01$  mag,  $18.96 \pm 0.01$  mag and  $18.63 \pm 0.01$  mag, respectively.

Simple Stellar Populations (SSPs) define the group/cluster of stars with the same age and chemical composition. SSPs are the most fundamental prediction of population synthesis models to determine the spectral evolution of stellar populations (Bruzual & Charlot 2003). Comparison of the integrated colors of individual clusters with SSPs gives an estimate of their ages. Here, we used  $U-B$ ,  $B-V$  and  $V-I$  colors of the cluster and compared with the SSP models with the color excess  $E(B-V)=0.15$  mag and metallicity of  $Z = 0.015$ .  $U-B$  and  $V-I$  colors were dereddened using the extinction coefficients from Sirianni et al. (2005). We derived the age of cluster as 6.73 Myr from SSP models.

The mass of this cluster was obtained from the extinction-corrected V-band luminosity and the age dependent mass-to-light ratio predicted by the SSP models with the metallicity and the distance modulus of 29.62 mag of the galaxy M51. We selected two-part *power-law* IMF (Initial Mass Function) from the models and found a total mass of  $\sim 3.2 \times 10^4 M_\odot$  with the age of 6.73 Myr for this cluster.

In addition, we constructed color-magnitude diagrams (CMDs) to determine ages and mass of the optical counterparts. Padova Stellar isochrones (PARSEC; Bressan et al. 2012) were used in CMD. We estimated the age of counterparts A and B as 9 Myr and 10 Myr, respectively. The masses are constrained as  $20 M_\odot$  for A and  $18 M_\odot$  for B.

## 3 RESULTS AND DISCUSSION

We investigated the X-ray and optical properties of ULX-4 in the Whirlpool galaxy M51 using archival *XMM-Newton*, *Chandra*, *Swift-XRT* and *HST* data spanning over 20 years. In the following sections, we discuss our main results.

### 3.1 X-Ray

We reanalyzed the majority of archival *XMM-Newton*, *Chandra* and *Swift-XRT* data sets noted earlier. Some of these data have not been used for spectral modelling and timing analysis in previous studies. Among the applied spectral models, an absorbed power-law model provided statistically acceptable fits to the *XMM-Newton*, *Chandra* datasets with an index of 1.44–2.0. This range is consistent with the source being in a hard state characterized by non-thermal emission (Remillard & McClintock 2006b; Feng & Kaaret 2009; Jin et al. 2010; Swartz et al. 2011; Koliopanos et al. 2019). Assuming accretion at Eddington luminosities, the mass of the compact object would be in the range 5–15  $M_\odot$  i.e., a stellar-mass BH.

The unfolded energy spectra of C12 data using *power-law* model is given in Fig.8. The profile of the spectrum is similar to that described as a hard ultra-luminous state by Sutton et al. (2013); Fabrika et al. (2021). The luminosity versus photon index for ULX-4 is shown in Fig.10. To investigate the possibility of a correlation between  $L_X$  and  $\Gamma$ , we determined the Spearman rank correlation coefficient ( $\rho$ ). We find a  $\rho$  value of -0.22 with a significance of 0.5. The magnitude of the coefficient is too small to suggest any significant correlation.

Nonetheless the source exhibits evidence for hard spectra especially for the *Chandra* data sets (black points). Although the uncertainties in the extracted  $\Gamma$  are relatively large, the *XMM-Newton* data sets, on the other hand, seem to show somewhat softer spectra (blue points). We now examine this particular feature in the data:

<sup>10</sup> <https://www.mathworks.com/matlabcentral/fileexchange/20129-fit-blackbody-equation-to-spectrum>

a number of *XMM-Newton* observations, notably, XM1, XM4 and XM5 (see Table 2), indicate the presence of the *mekal* component in the spectral fits in addition to the *power-law*. We used the F-test tool (in *XSPEC*) to determine whether the addition of this new component led to any improvement of the fits. We found F-test probabilities as  $10^{-5}$ , 0.17 and 0.23 for XM1, XM4 and XM5, respectively. These values indicate that the *power-law+mekal* model provides a statistically significant improvement only for XM1 data. Unfolded spectra of XM1 is shown in Fig. 9. We determined that the fraction of mekal component in the total flux from *power-law+mekal* is  $\sim 10\%$  in the 0.3–2 keV band for these three observations.

The presence of the *mekal* component could be in part due to emission originating from a hot diffuse thermal plasma (Feng & Kaaret 2005; Koliopanos et al. 2017). It is also notable that *Chandra* observations indicate the presence of point-like sources near ULX-4 which are not necessarily spatially resolved in the *XMM-Newton* data (see Fig. 3). These sources could add to the background seen in the ULX-4 spectra. In order to further probe whether the soft excess emission is intrinsic to ULX-4, we compared the excess flux in the 0.3–2 keV band modeled as a *power-law+mekal*, with the diffuse emission from its surrounding region. We estimated the flux of the diffuse emission from regions nearby ULX-4. For this, the *mekal* temperature of kT as 0.6 keV (as given in Table 2) was taken as an input for *WebPIMMS* tool. We found that the soft excess emission is comparable to the nearby diffuse emission. This implies that the soft excess emission is unlikely to be associated with ULX-4. This interpretation is consistent with the study of Dewangan et al. (2005) using the 2000–2001 *Chandra* and the 2003 *XMM-Newton* data for other ULXs (except source 69; ULX-7) in M51.

Using majority of the archival observations of *XMM-Newton*, *Chandra* and *Swift-XRT*, we obtained the long-term X-ray light curve of ULX-4 (see the left panel of Fig. 2).

As seen from Table 2, the spectral fitting results of data, we calculated the X-ray variability factor ( $V_f = F_{\max}/F_{\min}$ ) of ULX-4 as  $\sim 230$ . Here,  $F_{\max}$  and  $F_{\min}$  represent maximum and minimum of flux values, respectively. This factor was obtained by using the 2012 *Chandra* observations (C6 – C12) taken within a month. The source does not show significant variability from previously unused *Swift-XRT* observations (between MJD 57003 (2015) and MJD 59195 (2021)). We note that the propeller effect has been mentioned as a possible mechanism for the occurrence of high flux variability in ULXs (e.g. Tsygankov et al. 2016; Earnshaw et al. 2018, 2020b).

Earnshaw et al. (2018) and Song et al. (2020) have noted the existence of a bi-modal flux distribution in some ULXs, including also ULX-4. We have tested this scenario for ULX-4 by using the available data, and we find some evidence, in the *Chandra* data, for such a distribution (see the right panel of Fig. 2). We note at the same time that the statistics are very low and that the bi-modal feature is not evident in either the *XMM-Newton* or the *Swift-XRT* data sets. If the bi-modality feature is present then it may be indicative of a disk/wind precession. (Vinokurov et al. 2018; Weng & Feng 2018). Other possibilities discussed in the literature include; the propeller effect which requires the neutron star to have a very strong magnetic field (Illarionov & Sunyaev 1975; Tsygankov et al. 2016); binary systems in which the neutron star is typically in a moderately eccentric orbit ( $e < 0.5$ ) (Stella et al. 1986), or the change in the accretion rate via flow spherization as the system transition from the high to the low state (Grebenev 2017). In the framework of supercritical accretion, the wind emanating from the supercritical disk forms a funnel, which becomes visible during the precessional phases, thus leading to the visibility of a bright and spectrally hard X-ray source. In the other phases when the wind overlaps the channel

(the angle at which the disk and the wind are seen exceeds the opening angle of the channel), the luminosity will decrease by orders of magnitude. SS433 (Fabrika 2004; Poutanen et al. 2007; Weng & Feng 2018) is an example of such a process.

Given the relative hard spectra and the long-term flux variability indicated particularly by the *Chandra* data set (see black points; Fig. 2), it is possible that ULX-4 may in fact host a NS (Vinokurov et al. 2018; Rodríguez Castillo et al. 2020). Of course, we note that a pulsar-like signal has not been recorded. As noted by Ogawa et al. (2017), the absence of such a signal may be due to a line of sight highly inclined with respect to the binary system axis. Entertaining the NS scenario a little further, we can follow Tsygankov et al. (2016), and use the flux-variability factor  $V_f$  (determined earlier), to estimate the spin period (P) of the NS. We obtain  $\sim 1.5$  s using the relation  $\Delta L \sim 170P^{\frac{2}{3}} M_{1.4}^{\frac{1}{3}} R_6^{-1}$ , where  $M_{1.4}$  is the NS mass in units of  $1.4 M_{\odot}$ ,  $R_6$  is NS radius in units of  $10^6$  cm. This spin period is comparable to some known PULXs (e.g. X-2 in M82, X-1 in NGC 5907 and X-2 in NGC 1313) (Townsend & Charles 2020).

Focusing more on the long-term spectral evolution of ULX-4, we note the recent study of Gúrpide et al. (2021), in which they presented a hardness-luminosity diagram (HLD) for a sample of 17 ULXs (including PULXs) with archival data taken from *Chandra*, *XMM-Newton* and *NuSTAR*. This diagram is equivalent to the hardness-intensity diagram (HID) (Remillard & McClintock 2006a; Belloni 2010) that has been used for many years to probe the spectral evolution of galactic BH (and NS) binary systems and the internal coupling of the accretion process involving the corona and the accretion disk. A particular feature of the HID is the so-called q-curve shape that is traced out by BH transients as they undergo spectral transitions from the hard state through intermediate hard and soft states, to the soft state, and finally back down to the hard state. The primary aim of the HID, and other diagrams such as the color-color diagram (CCD) introduced by Done & Gierliński (2003), is to map the spectral transitions and, if possible, identify the nature of the compact object from the tracks they follow in the respective domains. In order to ascertain the position of ULX-4 on the HLD (HID), we imported the figure shown by upper panel of Gúrpide et al. (2021) (their Figure 4) onto which we plotted the hardness-luminosity values we extracted for ULX-4; the result is displayed in the Fig. 12. The *XMM-Newton* data are indicated as black stars and the *Chandra* set are denoted by red stars. The hardness was determined as the ratio of the unabsorbed fluxes in the hard (1.5 – 10 keV) to soft (0.3 – 1.5 keV) bands. As is seen in the upper panel of Fig. 12, ULX-4 occupies the lower section of the luminosity scale and the middle region of the hardness scale. However, according to the findings of Gúrpide et al. (2021), the majority of the confirmed PULXs reside in the region corresponding to higher luminosity and higher hardness. This would tend to suggest that the compact object in ULX-4 is either a stellar BH or a NS with a low magnetic field. Moreover, we note that the *XMM-Newton* points essentially cluster around an average hardness ratio of  $\sim 1.7$  and exhibit no discernible pattern. This is consistent with our discussion regarding the possible contribution of diffuse emission and unresolved background sources in the *XMM-Newton* spectra. In contrast, the *Chandra* points do show a hint of spectral evolution, with the hardness varying in the range  $\sim 1.1 - 4.1$ , and trace out what appears to be a partial q-curve-like track. Taken at face value this would argue for an ordinary stellar BH as the compact object in ULX-4. Clearly, the q-curve track is not complete and one would need additional data to draw a definite conclusion. In a similar fashion, we further probe the nature of



ULX-4 by deploying the CCD; in this case we define a hard color as the ratio of fluxes in the bands (5 - 8) and (2 - 5) keV, and a soft color as the ratio of fluxes in the bands (1 - 2) and (0.3 - 1) keV. Shown in the *bottom panel* of Fig. 12 is the resulting plot of hard color vs. soft color. We make a couple of observations regarding this result; the plot shows a diagonal track that is consistent with the one obtained by Done & Gierliński (2003) for a sample of galactic BH transients whose spectra are well described by a *power-law*. Secondly, they point out that the lower-left region of the plot (see their Figure 8) is only accessible to BH transients and not NS binaries (owing to the emission from the boundary layer between the NS surface and the inner part of the accretion disk). The ULX-4 points occupy precisely the noted region. This feature taken by itself would suggest that ULX-4 is more likely to be a transient BH than a NS.

### 3.2 Optical

We have identified two possible optical counterparts of ULX-4 using the *HST*/ACS and *HST*/WFC3 data. The two counterparts were detected within the astrometric error radius of  $0''.18$ . Their apparent magnitudes ( $m_V$ ) are between 23 - 23.5 mag and their absolute magnitude ( $M_V$ ) is  $\sim -6.6$  mag. These magnitudes are well in the range of other known ULXs (Tao et al. 2011; Gladstone et al. 2013; Vinokurov et al. 2018).

The spectral types of the counterparts A and B were estimated in two different ways: (1) Use of the CK04 models indicate both counterparts to be early B-type supergiants. As part of the same procedure, we identified the spectral types of two nearby field stars R1 and R2; these also turned out to be early B-type supergiants. (2) We made use of spectral fits using a blackbody function and obtained good fits to the SEDs and extracted temperatures of  $26554 \pm 104$  K and  $21386 \pm 173$  K for counterparts A and B respectively, with 95% confidence level. The fits for the counterparts and the field stars are shown in Fig. 5 and Fig. 6. The B-type nature of the counterparts were identified using the temperature and luminosity-class tables in Straizys & Kuriliene (1981). Considering the moderate periodic modulation of source A, we also checked the spectral type of the donor using data taken simultaneously with filters ACS/WFC/F435W, F555W and F814W. The approximation by the models of stellar atmospheres with these three points confirms that a shape of the energy distribution corresponds to a B type supergiant. The age and mass of the counterparts were determined as  $\sim 10$  Myr and  $\sim 20 M_\odot$ , respectively; the corresponding CMD is shown in Fig. 11. The B-type classification for the counterparts of ULX-4 is consistent with the general finding of OB-type giants as optical counterparts for other ULXs.

Interestingly, the classification of the field sources R1 and R2 also turns out to be the same as that for the counterparts A and B, suggesting the possibility that these sources are part of the same star cluster cataloged by Chandar et al. (2016). As seen from Fig. 4, the optical counterparts are located within 18 pc to a nearby cluster (where  $1''$  corresponds to  $\sim 44$  pc for the adopted distance of M51). We estimate the age of the cluster as 6.7 Myr and a mass as  $\sim 3.2 \times 10^4 M_\odot$ . Chandar et al. (2016) find  $\sim 6.8$  Myr and  $2.2 \times 10^4 M_\odot$  as the age and the mass respectively. There is excellent agreement on the age but the mass we extract is a little higher than given by Chandar et al. (2016). We suspect the small difference in the derived mass is likely due to fact that we used a larger aperture size, 8 pixels, in our photometry compared to the 2.5 pixels used by Chandar et al. (2016).

One of our more intriguing results is that the optical counterpart A appears to exhibit a low-amplitude periodic modulation of  $264 \pm 37$  days although it appears only in the F606W filter. We consider two possibilities for this apparent periodicity: one involves the nature of the donor and the other about the nature of the periodicity itself. In the first case, the optical modulation could result from the orbital motion of the donor which is distorted by the effects of gravity and is not irradiated equally by the X-ray radiation (Zampieri et al. 2012). Unfortunately, in this case the donor star can not be a B-type supergiant, since such a star is not likely to fill its Roche lobe assuming the periodicity is a result of the orbital period of several hundred days. Moreover, this implies the observed SED would have to be interpreted as a superposition of radiation from a hot wind, perhaps emanating from an accretion disk, and emission from a relatively cold donor. Such a donor may be a red supergiant (RSG) as has been noted in some ULX systems (Heida et al. 2019; López et al. 2020). In particular, by assuming Roche-lobe overflow, Heida et al. (2019) indicate that a red supergiant in NGC300 ULX-1 system is consistent with an orbital period in the range 0.8 - 2.1 years. This range accommodates the apparent periodicity we have found for ULX-4.

In the second scenario, we assume the donor is indeed a B-type (in fact a Be/X) star therefore there is no need for reassessing the nature of the SED but it calls into question the nature of the underlying cause for the observed periodicity. Here we note the results reported by Townsend & Charles (2020), where they display a reasonably tight positive correlation between the orbital period and the super-orbital period for a number of disk-fed high-mass X-ray binaries, Be/X binaries, and ULX pulsars. The super-orbital period is presumed to arise as the compact object interacts (regularly as part of its orbital motion) with a circumstellar disk of the donor and causes disturbances and/or obscurations in the medium of the disk which in turn propagate as density waves throughout the circumstellar disk causing a periodic feature in the observed optical light curves. This picture assumes that the periodicity we are witnessing is the super-orbital motion rather the ordinary orbit motion of the compact object. By assuming this scenario (i.e., a Be/X star since this class represents almost 60% of the high-mass X-ray binary population) and using the relation given by Townsend & Charles (2020), one can estimate the orbital period for the compact object to be  $\sim 10 - 15$  days. An interesting consequence of this scenario is that the compact object is highly likely to be a NS since we know that from over a 100 known galactic Be/X binaries only one has been shown to host a BH (see Brown et al. (2018), and Belczynski & Ziolkowski (2009)). Moreover, if the compact object is indeed a NS then it is most likely to be in the super-Eddington accretion regime. Of course, we recognize that both of the scenarios outlined above fall short of a definitive conclusion, a situation not entirely surprising given the limited quality data available for the analysis.

## 4 SUMMARY AND CONCLUSIONS

We have analyzed almost all the available X-ray data for the transient source, ULX-4, in M51. The data were taken from the *Chandra*, *XMM-Newton*, and *Swift-XRT* archives. In addition, we utilized optical data from the *HST* archives. The two main goals of the analysis were to a) determine the nature of ULX-4, and b) identify the optical counterpart(s) of the X-ray source. We performed relative astrometry between *Chandra* and *HST* data and identified two possible optical counterparts for ULX-4. By making use of FFTs and the construction of LS periodograms, both short-term and long-term

variability searches, including the extraction of spectral lags for the X-ray light curves, were carried out for both the X-ray and the optical data sets. X-ray spectra were extracted and limited spectral analysis was done by deploying simple spectral models such as the *power-law* in order to ascertain and describe the main spectral features of the data. Additional spectral analysis of the X-ray data included the extraction of hardness ratios and the construction of color-color diagrams to identify possible spectral transitions of the source and to delineate the nature of the compact object in ULX-4. For the optical data, we constructed SEDs which were then fitted with a blackbody model to constrain the temperatures and obtain spectral types for the optical counterparts. CMDs were created to obtain the mass and age of the optical counterparts. Our main findings from this study are summarized as follows:

- We have identified two optical counterparts (labelled as A and B) for ULX-4; the age and mass of A is 9 Myr and 20  $M_{\odot}$  respectively; that of B is 10 Myr and 18  $M_{\odot}$  respectively,
- Based on the optical SEDs, the temperatures for the counterparts are  $(26554 \pm 104)$  K for A and  $(21386 \pm 173)$  K for B, suggesting a spectral type in the range B0I and B3I (but see note about optical variability down below),
- Counterpart A exhibits a low-amplitude optical periodicity of  $264 \pm 37$  days in the F606W filter; no periodicity was found for counterpart B,
- If we assume the apparent periodicity seen in A is associated with the orbital motion of the donor then the donor is more likely a red RSG in order to satisfy the long periodicity and the need to accommodate Roche-lobe overflow. As a consequence, the SED would then have to be interpreted as a superposition of emissions from a cold donor and a hot flow component most likely from an accretion disk. If, on the other hand, the periodicity is super-orbital in nature i.e., due to interactions of the compact object with a circumstellar disk, then the donor could be a Be/X star with the compact object being a NS,
- The majority of the X-ray data are best described by a simple *power-law* with an index in the range 1.44 - 2.0; a couple of *XMM-Newton* observations indicate the presence of a soft component which are best described with the addition of a *mekal* component suggesting a contribution from a diffuse background source,
- We find some evidence for the existence of a bi-modal distribution of the X-ray flux of ULX-4, the cause of which is of some debate in the literature (Illarionov & Sunyaev 1975; Stella et al. 1986; Vinokurov et al. 2018)
- The HID, the CCD, along with the significant variability noted in the long-term X-ray light curve from *Chandra*, present a rather mixed picture as to the nature of ULX-4 i.e., arguments could be advanced for either a stellar-size BH or a low-magnetic field NS. Unfortunately, the data are incomplete and/or of low statistics thus rendering a definitive conclusion speculative at best.
- Finally, as a side product of this study, we note the presence of a previously uncatalogued (transit) X-ray source (CXOU J132951.7 +471010) in a number of *Chandra* observations. The unabsorbed flux of this new source in the range of  $(0.05-1.88) \times 10^{-14}$  erg cm $^{-2}$  s $^{-1}$ .

## 5 ACKNOWLEDGEMENTS

This research was supported by the Scientific and Technological Research Council of Turkey (TÜBİTAK) through project number 117F115. This research is a part of the PhD thesis of S. Allak

and he acknowledges financial support by TÜBİTAK. ES and KD acknowledges support provided by the Scientific and Technological Research Council of Turkey (TÜBİTAK) through project number 119F334. We thank the TÜBİTAK National Observatory (TUG) for support with observing times and equipment. Astrometry was performed as part of the government contract of the SAO RAS approved by the Ministry of Science and Higher Education of the Russian Federation. The study of the nature of optical radiation was supported by the Russian Science Foundation (project no. 21-72-10167 ULXs: wind and donors). Finally, we acknowledge the useful comments and recommendations of the Referee which helped to clarify a number of issues.

## DATA AVAILABILITY

The scientific results reported in this article are based on archival observations made by the *Chandra*<sup>11</sup>, *XMM-Newton*<sup>12</sup> and *Swift-XRT*<sup>13</sup> X-ray Observatories. This work has also made use of observations made with the NASA/ESA Hubble Space Telescope, and obtained from the data archive at the Space Telescope Science Institute<sup>14</sup>

## REFERENCES

- Aksaker N., Akyuz A., Avdan S., Avdan H., 2019, *MNRAS*, **488**, 5935  
Akyuz A., Avdan S., Allak S., Aksaker N., Akkaya Oralhan I., Balman S., 2020, *MNRAS*, **499**, 2138  
Allak S., Akyuz A., Aksaker N., Ozdogan Ela M., Avdan S., Soyduğan F., 2020, *MNRAS*, **499**, 5682  
Avdan S., et al., 2019, *ApJ*, **875**, 68  
Bachetti M., et al., 2014, *Nature*, **514**, 202  
Bahramian A., Kennea J. A., Shaw A. W., 2017, *The Astronomer's Telegram*, **10866**, 1  
Barnard R., Garcia M., Murray S. S., 2013, *ApJ*, **772**, 126  
Beardmore A. P., et al., 2017, GRB Coordinates Network, **21971**, 1  
Belczynski K., Ziolkowski J., 2009, *ApJ*, **707**, 870  
Belloni T. M., 2010, *States and Transitions in Black Hole Binaries*. Springer, p. 53, doi:10.1007/978-3-540-76937-8\_3  
Beri A., et al., 2021, *MNRAS*, **500**, 565  
Block D. L., Elmegreen B. G., Stockton A., Sauvage M., 1997, *ApJ*, **486**, L95  
Bressan A., Marigo P., Girardi L., Salasnich B., Dal Cero C., Rubele S., Nanni A., 2012, *MNRAS*, **427**, 127  
Brightman M., et al., 2018, *Nature Astronomy*, **2**, 312  
Brightman M., et al., 2019, *ApJ*, **873**, 115  
Brightman M., et al., 2020, *ApJ*, **895**, 127  
Brown R. O., Ho W. C. G., Coe M. J., Okazaki A. T., 2018, *MNRAS*, **477**, 4810  
Bruzual G., Charlot S., 2003, *MNRAS*, **344**, 1000B  
Cardelli J. A., Wallerstein G., 1989, *AJ*, **97**, 1099  
Carpano S., Haberl F., Maitra C., Vasilopoulos G., 2018, *MNRAS*, **476**, L45  
Castelli F., Kurucz R. L., 2004, *A&A*, **419**, 725  
Chandar R., Whitmore B. C., Dinino D., Kennicutt R. C., Chien L. H., Schinnerer E., Meidt S., 2016, *ApJ*, **824**, 71  
Colbert E. J. M., Mushotzky R. F., 1999, *ApJ*, **519**, 89  
Colbert E. J. M., Ptak A. F., 2002, *ApJS*, **143**, 25  
De Marco B., Ponti G., Miniutti G., Belloni T., Cappi M., Dadina M., Muñoz-Darias T., 2013, *MNRAS*, **436**, 3782

<sup>11</sup> <https://cda.harvard.edu/chaser/>

<sup>12</sup> <http://nxsa.esac.esa.int/nxsa-web/>

<sup>13</sup> [https://www.swift.ac.uk/swift\\_portal/](https://www.swift.ac.uk/swift_portal/)

<sup>14</sup> <https://mast.stsci.edu/portal/Mashup/Clients/Mast/Portal.html>

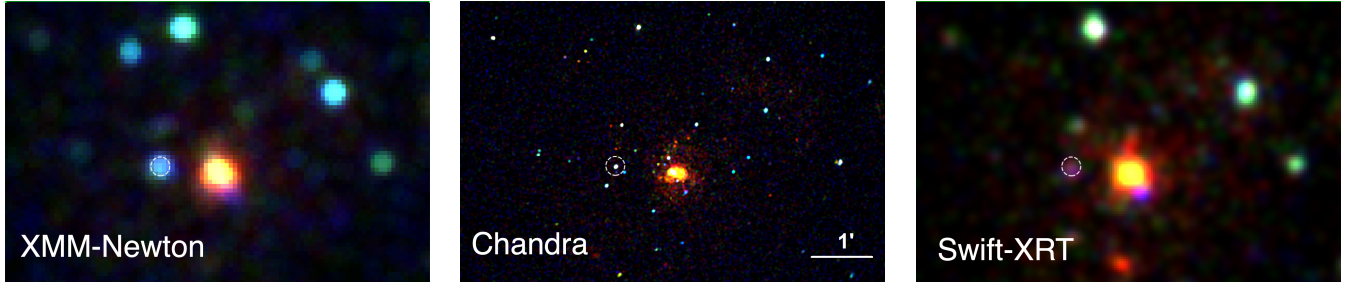


**Figure 1.** X-ray true color (Red :0.3-1 keV, Green: 1-2 keV and Blue: 2-7 keV) images of ULX-4. left panel: *XMM-Newton* (XM5), center panel: *Chandra* (C12) and right panel: *Swift-XRT* (stacked images: observations of Target ID 30083). The images were smoothed with a 3'' Gaussian. The source ULX-4 is indicated by dashed white circles. All three images show the same region ( $4.9' \times 7.4'$ ). North is left and east is up in all panels.

**Table 1.** X-ray observations log for ULX-4 in M51

Observatory	Label	ObsID	Instrument	Date (YYYY-MM-DD)	Exp. (ks)
<i>XMM-Newton</i>	XM1	0212480801	EPIC	2005-07-01	49.21
	XM2	0303420101	EPIC	2006-05-20	54.11
	XM3	0303420201	EPIC	2006-05-24	36.81
	XM4	0677980701	EPIC	2011-06-07	13.32
	XM5	0677980801	EPIC	2011-06-11	13.32
	XM6	0830191501	EPIC	2018-06-13	63.00
	XM7	0830191601	EPIC	2018-06-15	63.00
	XM8	0852030101	EPIC	2019-07-11	77.00
<i>Chandra</i>	C1	354	ACIS-S	2000-06-20	14.86
	C2	1622	ACIS-S	2001-06-23	26.81
	C3	3932	ACIS-S	2003-08-07	47.97
	C4	12562	ACIS-S	2011-06-12	9.63
	C5	12668	ACIS-S	2011-07-03	9.99
	C6	13813	ACIS-S	2012-09-09	179.20
	C7	13812	ACIS-S	2012-09-12	157.46
	C8	15496	ACIS-S	2012-09-19	40.97
	C9	13814	ACIS-S	2012-09-20	189.85
	C10	13815	ACIS-S	2012-09-23	67.18
	C11	13816	ACIS-S	2012-09-26	73.10
	C12	15553	ACIS-S	2012-10-10	37.57
	C13	19522	ACIS-I	2017-03-17	37.76
	C14	20998	ACIS-S	2018-08-31	19.82

Dewangan G. C., Griffiths R. E., Choudhury M., Miyaji T., Schurch N. J., 2005, *ApJ*, **635**, 198  
 Dickey J. M., Lockman F. J., 1990, *ARA&A*, **28**, 215  
 Done C., Gierliński M., 2003, *MNRAS*, **342**, 1041  
 Earnshaw H. P., Roberts T. P., Sathyaprakash R., 2018, *MNRAS*, **476**, 4272  
 Earnshaw H. P., et al., 2020a, in American Astronomical Society Meeting Abstracts. American Astronomical Society Meeting Abstracts. p. 237.02  
 Earnshaw H. P., et al., 2020b, *ApJ*, **891**, 153  
 Evans P. A., et al., 2009, *MNRAS*, **397**, 1177  
 Fabrika S., 2004, *Astrophys. Space Phys. Res.*, **12**, 1  
 Fabrika S. N., Atapin K. E., Vinokurov A. S., Sholukhova O. N., 2021, *Astrophysical Bulletin*, **76**, 6  
 Feng H., Kaaret P., 2005, *ApJ*, **633**, 1052  
 Feng H., Kaaret P., 2009, *ApJ*, **696**, 1712  
 Fürst F., et al., 2016, *ApJ*, **831**, L14  
 Fürst F., Walton D. J., Stern D., Bachetti M., Barret D., Brightman M., Harrison F. A., Rana V., 2017, *ApJ*, **834**, 77  
 Ghosh T., Rana V., 2021, *MNRAS*, **504**, 974  
 Gladstone J. C., Roberts T. P., Done C., 2009, *MNRAS*, **397**, 1836  
 Gladstone J. C., Copperwheat C., Heinke C. O., Roberts T. P., Cartwright T. F., Levan A. J., Goad M. R., 2013, *ApJS*, **206**, 14

Grebenev S. A., 2017, *Astronomy Letters*, **43**, 464  
 Gúrpide A., Godet O., Koliopanos F., Webb N., Olive J. F., 2021, *A&A*, **649**, A104  
 Heida M., et al., 2019, *ApJ*, **883**, L34  
 Heil L. M., Vaughan S., 2010, *MNRAS*, **405**, L86  
 Hernández-García L., Vaughan S., Roberts T. P., Middleton M., 2015, *MNRAS*, **453**, 2877  
 Horesh A., et al., 2013, *MNRAS*, **436**, 1258  
 Hu C.-P., Kong A. K. H., Ng C. Y., Li K. L., 2018, *ApJ*, **864**, 64  
 Huppenkothen D., et al., 2019a, *The Journal of Open Source Software*, **4**, 1393  
 Huppenkothen D., et al., 2019b, *ApJ*, **881**, 39  
 Illarionov A. F., Sunyaev R. A., 1975, *A&A*, **39**, 185  
 Israel G. L., et al., 2017a, *Science*, **355**, 817  
 Israel G. L., et al., 2017b, *MNRAS*, **466**, L48  
 Jaisawal G. K., Naik S., Chenevez J., 2018, *MNRAS*, **474**, 4432  
 Jenke P., Wilson-Hodge C. A., 2017, *The Astronomer's Telegram*, **10812**, 1  
 Jin J., Feng H., Kaaret P., 2010, *ApJ*, **716**, 181  
 Kaaret P., Feng H., Roberts T. P., 2017, *ARA&A*, **55**, 303  
 Kara E., et al., 2020, *MNRAS*, **491**, 5172  
 Kennea J. A., Lien A. Y., Krimm H. A., Cenko S. B., Siegel M. H., 2017,



**Table 2.** X-Ray spectral fitting parameters of ULX-4.

Label (1)	Count rate (2)	N <sub>PL</sub> (3)	N <sub>mekal</sub> (4)	Γ (5)	kT (6)	F <sub>X</sub> (7)	L <sub>X</sub> (8)	χ <sup>2</sup> /dof (χ <sub>V</sub> <sup>2</sup> ) (9)
Model: <i>tbabs</i> × <i>power-law</i>								
C1	<0.11	...	...	...	...	<0.04	<0.04	...
C2	23.87 ± 0.96	2.40 <sup>+0.19</sup> <sub>-0.19</sub>	...	1.44 <sup>+0.11</sup> <sub>-0.11</sub>	...	2.12 <sup>+0.15</sup> <sub>-0.15</sub>	2.05 <sup>+0.14</sup> <sub>-0.14</sub>	54.51/53(1.03)
C3	<0.06	...	...	...	...	<0.02	<0.02	...
C4	10.59 ± 1.09	1.52 <sup>+0.36</sup> <sub>-0.34</sub>	...	1.95 <sup>+0.32</sup> <sub>-0.32</sub>	...	0.88 <sup>+0.17</sup> <sub>-0.17</sub>	0.85 <sup>+0.16</sup> <sub>-0.16</sub>	15.76/15(1.05)
C5	0.35 ± 0.02	...	...	...	...	0.05 ± 0.02	0.05 ± 0.02	...
C6	0.13 ± 0.06	...	...	...	...	0.014 ± 0.007	0.02 ± 0.01	...
C7	0.10 ± 0.04	...	...	...	...	0.011 ± 0.006	0.01 ± 0.01	...
C8	0.07 ± 0.02	...	...	...	...	0.007 ± 0.0004	0.01 ± 0.01	...
C9	0.14 ± 0.08	...	...	...	...	0.02 ± 0.01	0.02 ± 0.01	...
C10	0.15 ± 0.02	...	...	...	...	0.02 ± 0.01	0.02 ± 0.01	...
C11	3.24 ± 0.23	0.44 <sup>+0.07</sup> <sub>-0.07</sub>	...	1.65 <sup>+0.23</sup> <sub>-0.22</sub>	...	0.32 <sup>+0.04</sup> <sub>-0.04</sub>	0.31 <sup>+0.04</sup> <sub>-0.04</sub>	34.65/43(0.81)
C12	22.41 ± 0.79	3.45 <sup>+0.25</sup> <sub>-0.25</sub>	...	1.75 <sup>+0.10</sup> <sub>-0.10</sub>	...	2.29 <sup>+0.14</sup> <sub>-0.14</sub>	2.21 <sup>+0.13</sup> <sub>-0.13</sub>	63.77/66(0.96)
C13	0.13 ± 0.02	...	...	...	...	0.03 ± 0.01	0.03 ± 0.01	...
C14	8.58 ± 0.69	1.81 <sup>+0.44</sup> <sub>-0.42</sub>	...	1.78 <sup>+0.30</sup> <sub>-0.29</sub>	...	1.16 <sup>+0.17</sup> <sub>-0.17</sub>	1.13 <sup>+0.16</sup> <sub>-0.16</sub>	31.41/28(1.12)
XM1	39.20 ± 1.51	2.52 <sup>+0.15</sup> <sub>-0.15</sub>	...	1.85 <sup>+0.11</sup> <sub>-0.11</sub>	...	1.55 <sup>+0.09</sup> <sub>-0.09</sub>	1.50 <sup>+0.09</sup> <sub>-0.09</sub>	126.63/83(1.53)
XM2	21.60 ± 1.45	1.36 <sup>+0.13</sup> <sub>-0.13</sub>	...	2.00 <sup>+0.19</sup> <sub>-0.19</sub>	...	0.76 <sup>+0.07</sup> <sub>-0.07</sub>	0.74 <sup>+0.07</sup> <sub>-0.07</sub>	59.71/69(0.87)
XM3*	9.21 ± 1.10	...	...	...	...	0.25 ± 0.03	0.24 ± 0.03	...
XM4	50.60 ± 2.61	3.14 <sup>+0.28</sup> <sub>-0.29</sub>	...	1.90 <sup>+0.17</sup> <sub>-0.17</sub>	...	1.87 <sup>+0.12</sup> <sub>-0.12</sub>	1.81 <sup>+0.11</sup> <sub>-0.11</sub>	23.64/15(1.58)
XM5	31.90 ± 4.75	1.84 <sup>+0.38</sup> <sub>-0.38</sub>	...	1.73 <sup>+0.47</sup> <sub>-0.47</sub>	...	1.23 <sup>+0.26</sup> <sub>-0.26</sub>	1.19 <sup>+0.25</sup> <sub>-0.25</sub>	24.26/29(0.84)
XM6	18.90 ± 0.80	1.27 <sup>+0.09</sup> <sub>-0.09</sub>	...	1.86 <sup>+0.12</sup> <sub>-0.12</sub>	...	0.78 <sup>+0.06</sup> <sub>-0.06</sub>	0.75 <sup>+0.05</sup> <sub>-0.05</sub>	51.94/38(1.37)
XM7	17.40 ± 0.78	1.07 <sup>+0.09</sup> <sub>-0.08</sub>	...	1.84 <sup>+0.14</sup> <sub>-0.14</sub>	...	0.60 <sup>+0.05</sup> <sub>-0.05</sub>	0.59 <sup>+0.05</sup> <sub>-0.05</sub>	19.17/20(0.96)
XM8*	9.52 ± 0.63	...	...	...	...	0.26 ± 0.02	0.25 ± 0.02	...
Model: <i>tbabs</i> × ( <i>power-law</i> + <i>mekal</i> )								
XM1	...	1.99 <sup>+0.15</sup> <sub>-0.15</sub>	5.17 <sup>+1.06</sup> <sub>-1.06</sub>	1.68 <sup>+0.13</sup> <sub>-0.13</sub>	0.59 <sup>+0.17</sup> <sub>-0.17</sub>	1.55 <sup>+0.05</sup> <sub>-0.05</sub>	1.50 <sup>+0.09</sup> <sub>-0.09</sub>	99.37/81(1.23)
XM4	...	2.43 <sup>+0.36</sup> <sub>-0.36</sub>	8.38 <sup>+4.89</sup> <sub>-4.89</sub>	1.57 <sup>+0.32</sup> <sub>-0.32</sub>	0.30 <sup>+0.26</sup> <sub>-0.26</sub>	2.08 <sup>+0.08</sup> <sub>-0.08</sub>	2.02 <sup>+0.08</sup> <sub>-0.08</sub>	18.05/13(1.39)
XM5	...	1.18 <sup>+0.33</sup> <sub>-0.33</sub>	7.63 <sup>+3.77</sup> <sub>-3.77</sub>	1.10 <sup>+0.29</sup> <sub>-0.29</sub>	0.25 <sup>+0.10</sup> <sub>-0.10</sub>	1.83 <sup>+0.08</sup> <sub>-0.12</sub>	1.77 <sup>+0.11</sup> <sub>-0.10</sub>	21.78/27(0.80)

Note. — Col. (1): Observation label corresponding to Column (1) of Table 1. Col. (2): Source count rates in units of 10<sup>-3</sup> counts s<sup>-1</sup> in 0.3–10 keV. Col. (3): N<sub>PL</sub> is the normalization of the *power-law* model at 1 keV in units of 10<sup>-5</sup> photons cm<sup>-2</sup> s<sup>-1</sup>. Col. (4): N<sub>mekal</sub> is the normalization of the *mekal* model in units of 10<sup>-6</sup> × 10<sup>-14</sup> 4πD<sup>2</sup> n<sub>e</sub>n<sub>H</sub>dV where D is the angular diameter distance to the source (cm), n<sub>e</sub> and n<sub>H</sub> are the electron and H densities (cm<sup>-3</sup>), respectively. Col. (5): Γ is the photon index of the *power-law* model. Col. (6): Plasma temperature in unit of keV. Col. (7): Unabsorbed flux in units of 10<sup>-13</sup> ergs cm<sup>-2</sup> s<sup>-1</sup>. Col. (8): Unabsorbed luminosity in units of 10<sup>39</sup> ergs s<sup>-1</sup>. Col. (9): Best-fit χ<sup>2</sup> and degrees of freedom. The χ<sub>V</sub><sup>2</sup> is given in parentheses. All errors are at 90% confidence level. Unabsorbed flux and luminosity values were calculated in the 0.3–10 keV energy band. Adopted distance of 9 Mpc (Rodríguez et al. 2014; Song et al. 2020) was used for luminosity. \*Since both XM3 and XM8 have insufficient data the source fluxes were calculated using the Webpimms tool with a photon index of Γ = 1.75 and N<sub>H</sub> = 0.03 × 10<sup>22</sup> cm<sup>2</sup>. Except for XM1, simultaneous fit of EPIC pn + MOS spectra for the remaining datasets did not give us acceptable parameters for a single and two component models. Only the X-ray absorption value N<sub>H</sub> = 0.03 × 10<sup>22</sup> cm<sup>2</sup> as used for all spectra and this value was kept fixed.

**Table 3.** The log of *HST*/ACS and WFC3 observations.

Instrument	Filter	ObsID	Date (YYYY-MM-DD)	Exp. (s)
ACS/WFC	F435W	J97C51R3Q	2005-01-20	340
ACS/WFC	F555W	J97C51R4Q	2005-01-20	340
ACS/WFC	F814W	J97C51R6Q	2005-01-20	340
ACS/WFC3	F275W	ICD401010	2014-09-11	1400
ACS/FWC3	F336W	ICD401020	2014-09-11	1450
ACS/WFC	F606W	JD8F01010	2016-10-05	2200

The Astronomer’s Telegram, 10809, 1  
King A., Lasota J.-P., 2020, *MNRAS*, 494, 3611  
Koliopanos F., Vasilopoulos G., Godet O., Bachetti M., Webb N. A., Barret D., 2017, *A&A*, 608, A47

Koliopanos F., Vasilopoulos G., Buchner J., Maitra C., Haberl F., 2019, *A&A*, 621, A118  
Kuntz K. D., Long K. S., Kilgard R. E., 2016, *ApJ*, 827, 46  
Liu J., Bregman J. N., McClintock J. E., 2009, *ApJ*, 690, L39  
Lomb N. R., 1976, *Ap&SS*, 39, 447  
López K. M., Heida M., Jonker P. G., Torres M. A. P., Roberts T. P., Walton D. J., Moon D. S., Harrison F. A., 2020, *MNRAS*, 497, 917  
Mezcua M., 2017, *International Journal of Modern Physics D*, 26, 1730021  
Middleton M. J., Sutton A. D., Roberts T. P., Jackson F. E., Done C., 2012, *MNRAS*, 420, 2969  
Miller M. C., Lamb F. K., Psaltis D., 1998, *ApJ*, 508, 791  
Motch C., Pakull M. W., Soria R., Grisé F., Pietrzyński G., 2014, *Nature*, 514, 198  
Mucciarelli P., Zampieri L., Treves A., Turolla R., Falomo R., 2007, *ApJ*, 658, 999  
Ogawa T., Mineshige S., Kawashima T., Ohsuga K., Hashizume K., 2017, *PASJ*, 69, 33  
Osheroich V., Titarchuk L., 1999, *ApJ*, 522, L113  
Osterbrock D. E., 1989, *Astrophysics of gaseous nebulae and active galactic*

**Table 4.** Coordinates of the X-ray/optical reference sources.

Source.	<i>Chandra</i> R.A. (hh:mm:ss.sss)	<i>Chandra</i> Dec. (° : ' : ")	Counts <sup>a</sup> -	<i>HST</i> R.A. (hh:mm:ss.sss)	<i>HST</i> Dec. (° : ' : ")	
<i>Chandra</i> ACIS-S X-ray sources (ObsID 13816) identified in <i>HST</i> observation (J97C51R4Q)						Offset(")
SN 2011dh	13:30:05.108	+47:10:11.10	79.25 ± 10.63	13:30:05.104	+47:10:10.89	0.21
XOUJ133006.5+470834	13:30:06.456	+47:08:34.86	348.71 ± 21.74	13:30:06.446	+47:08:34.72	0.17
J133011+471041	13:30:11.023	+47:10:41.24	143.93 ± 14.57	13:30:11.009	+47:10:41.14	0.18
<i>Chandra</i> and corrected optical coordinates of optical counterparts						Position uncertainty (")
ULX-4	13:29:53.333	+47:10:42.76	...	13:29:53.323	+47:10:42.64	0.18

Note. — <sup>a</sup>: The *Chandra* counts were calculated in the 0.3–10 keV using *XSPEC*

**Table 5.** The dereddened Vega magnitudes and flux values of optical counterparts of ULX-4

Filter	Pivot Wavelength <sup>a</sup> (Å)	ZP <sup>b</sup> (mag)	Aperture corr. (mag)	Vega Magnitude		Flux ( $10^{-14}$ erg s <sup>-1</sup> cm <sup>-2</sup> )	
				A	B	A	B
F275W	2710.4	22.66	0.43	21.25 ± 0.03	21.96 ± 0.04	6.78 ± 0.04	3.53 ± 0.05
F336W	3354.8	23.46	0.38	21.45 ± 0.04	22.17 ± 0.04	5.10 ± 0.04	2.63 ± 0.05
F435W	4329.8	25.77	0.35	23.17 ± 0.04	23.67 ± 0.05	2.25 ± 0.04	1.42 ± 0.05
F555W	5360.8	25.71	0.27	23.12 ± 0.04	23.40 ± 0.05	1.55 ± 0.04	1.22 ± 0.05
F606W	5921.0	26.41	0.26	23.17 ± 0.04	23.67 ± 0.04	0.75 ± 0.04	0.72 ± 0.05
F814W	8044.8	25.52	0.28	23.19 ± 0.04	23.35 ± 0.05	0.62 ± 0.04	0.50 ± 0.05

Note. — <sup>a</sup> pivot wavelengths and <sup>b</sup> Zeropoint Vega magnitude of filters were calculated with *PYSYNPHOT*.

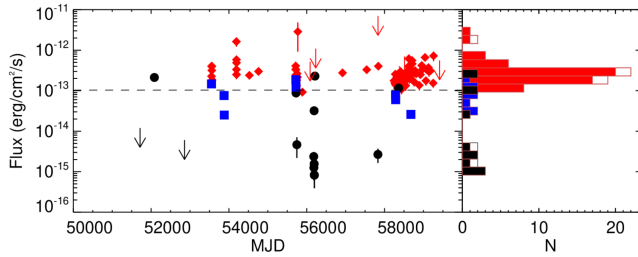


**Figure 2.** The long-term X-ray light curves of ULX-4 (left) and the histogram panel (right). *Chandra*, *XMM-Newton* and *Swift-XRT* observations are marked filled black circles, blue squares and red diamonds, respectively.  $3\sigma$  upper limits for *Chandra* and *Swift-XRT* data are shown by the black and red downward arrows, respectively and also they are shown with open squares in the histogram

. For the histogram *Swift-XRT* observations are binned with 10-day binning. N is the number of observations. Dashed black line indicates the flux threshold for ULX state.

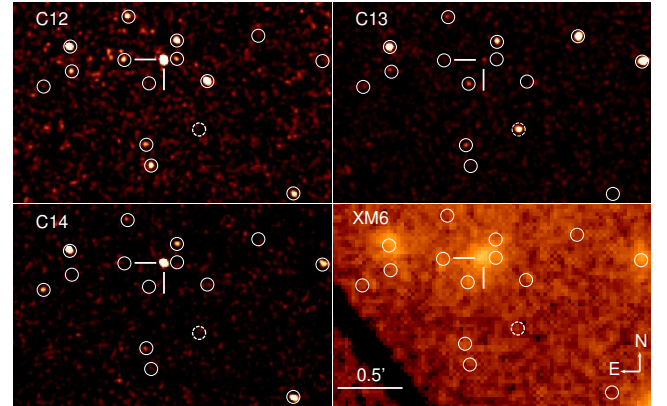


**Figure 3.** Comparisons of ULX-4 (white bars) and new transient source CXOU J132951.7+471010 (dashed white circle) in C12 (2012), C13 (2017), C14 (2018) and XM6 (2018) observations, respectively. White circles with a radius of  $3''$  represent some of the X-ray sources cataloged by Kuntz et al. (2016). All panels were obtained with the same scale and the images were Gaussian smoothed with a radius of  $3''$ .

nuclei. University Science Books  
 Ozdogan Ela M., et al., 2021, *MNRAS*, **505**, 771  
 Pinto C., et al., 2017, *MNRAS*, **468**, 2865  
 Pintore F., et al., 2020, *ApJ*, **890**, 166  
 Pintore F., et al., 2021, *MNRAS*, **504**, 551  
 Poutanen J., Lipunova G., Fabrika S., Butkevich A. G., Abolmasov P., 2007, *MNRAS*, **377**, 1187  
 Rampadarath H., Morgan J. S., Soria R., Tingay S. J., Reynolds C., Argo M. K., Dumas G., 2015, *MNRAS*, **452**, 32  
 Remillard R. A., McClintock J. E., 2006a, *ARA&A*, **44**, 49  
 Remillard R. A., McClintock J. E., 2006b, in American Astronomical Society Meeting Abstracts. p. 07.05

Roberts T. P., Warwick R. S., 2000, *MNRAS*, **315**, 98  
 Rodríguez Castillo G. A., et al., 2020, *ApJ*, **895**, 60  
 Rodríguez Ó., Clocchiatti A., Hamuy M., 2014, *AJ*, **148**, 107  
 Sathyaprakash R., et al., 2019, *MNRAS*, **488**, L35  
 Scargle J. D., 1982, *ApJ*, **263**, 835  
 Sirianni M., et al., 2005, *PASP*, **117**, 1049  
 Song X., Walton D. J., Lansbury G. B., Evans P. A., Fabian A. C., Earnshaw H., Roberts T. P., 2020, *MNRAS*, **491**, 1260  
 Soria R., Cropper M., Pakull M., Mushotzky R., Wu K., 2005, *MNRAS*,

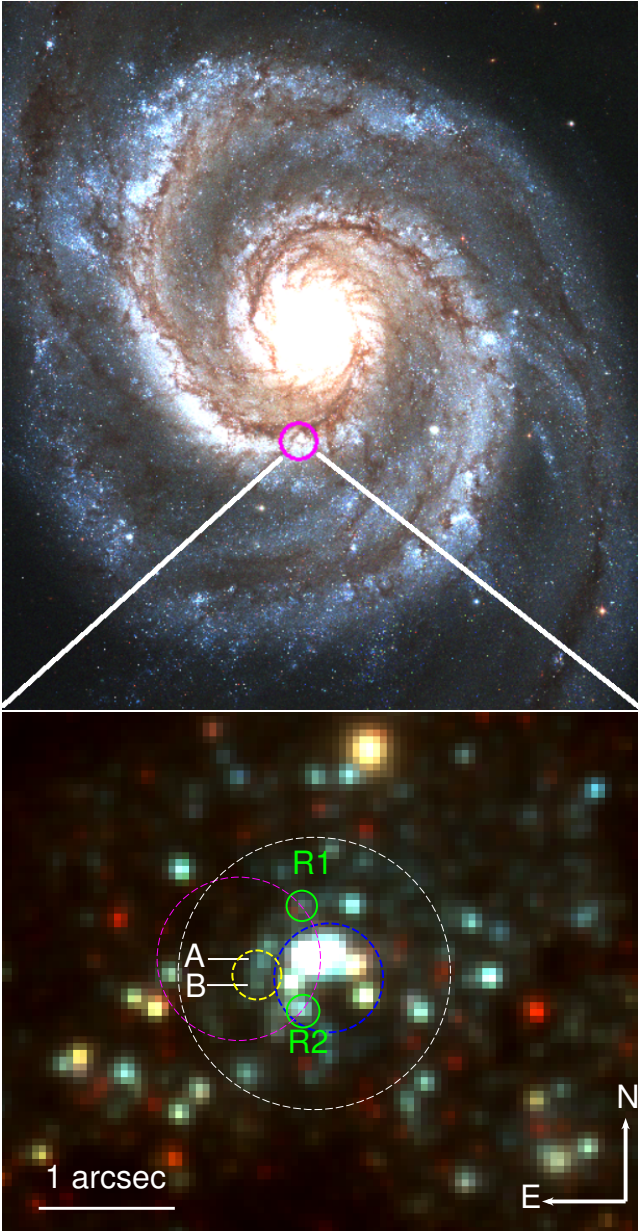


**Figure 4.** The *HST* RGB image (R:F814W, G:F555W and B:F435W) of ULX-4 and its environment. The dashed magenta circle represents the *Chandra* position of ULX-4 with a radius of  $0''.6$ . The dashed yellow circle represents the astrometric corrected coordinates of ULX-4. The optical counterparts A and B are also shown with white bars. The dashed blue circle indicates the star cluster. The dashed white circle represents the region used for reference sources with a  $1''$  radius. Also, two field stars (R1 and R2) are shown with green circles which are used for SEDs.

356, 12

- Stella L., Vietri M., 1999, *Phys. Rev. Lett.*, **82**, 17  
 Stella L., White N. E., Rosner R., 1986, *ApJ*, **308**, 669  
 Stetson P. B., 1987, *PASP*, **99**, 191  
 Straizys V., Kuriliene G., 1981, *Ap&SS*, **80**, 353  
 Sutton A. D., Roberts T. P., Middleton M. J., 2013, *MNRAS*, **435**, 1758  
 Swartz D. A., Soria R., Tennant A. F., Yukita M., 2011, *ApJ*, **741**, 49  
 Tao L., Feng H., Gris   F., Kaaret P., 2011, *ApJ*, **737**, 81  
 Terashima Y., Wilson A. S., 2004, *ApJ*, **601**, 735  
 Terashima Y., Inoue H., Wilson A. S., 2006, *ApJ*, **645**, 264

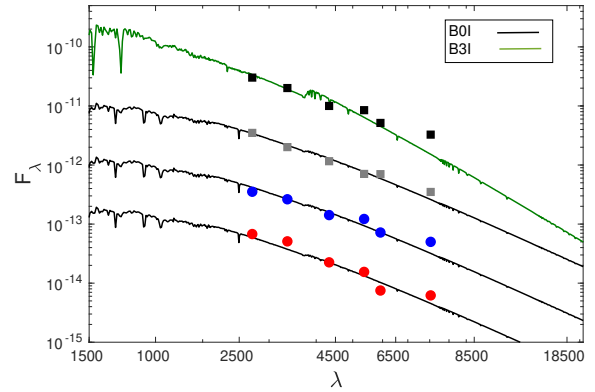


**Figure 5.** The SEDs of optical counterparts A and B with field stars R1 and R2. The black and green lines represent the synthetic spectra for B0I and B3I, respectively. The red and blue filled circles represent flux values of counterparts for A and B, respectively. The filled black and gray squares represent flux values of sources for R1 and R2, respectively. All SEDs were derived with metallicity of  $Z_{\odot} = 0.02$  and extinction of  $A_V = 0.46$  mag. Systematic errors are less than 4%. The lines were shifted upward by factor of 10 for clarity. The units of y and x axes are  $\text{erg s}^{-1} \text{cm}^{-2}$  and  $\text{\AA}$ , respectively.

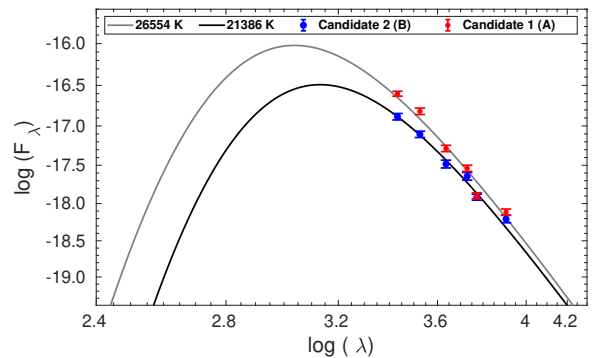


**Figure 6.** The reddening corrected SEDs of optical counterparts A (red circles) and B (blue circles). The solid lines indicate blackbody models fitted to the available wavelength points, with temperatures of 26554 K for A and 21386 K for B. The units of y and x axes are  $\text{erg s}^{-1} \text{cm}^{-2} \text{\AA}^{-1}$  and  $\text{\AA}$ , respectively.

- Titarchuk L., Seifina E., 2016, *A&A*, **595**, A101  
 Townsend L. J., Charles P. A., 2020, *MNRAS*, **495**, 139  
 Tsygankov S. S., Mushtukov A. A., Suleimanov V. F., Poutanen J., 2016, *MNRAS*, **457**, 1101  
 Urquhart R., Soria R., 2016, *ApJ*, **831**, 56  
 Urquhart R., Soria R., Johnston H. M., Pakull M. W., Motch C., Schwoppe A., Miller-Jones J. C. A., Anderson G. E., 2018, *MNRAS*, **475**, 3561  
 Uttley P., Cackett E. M., Fabian A. C., Kara E., Wilkins D. R., 2014, *A&ARv*, **22**, 72  
 Villar V. A., et al., 2016, *ApJ*, **830**, 11  
 Vinokurov A., Fabrika S., Atapin K., 2018, *ApJ*, **854**, 176  
 Vinokurov A., Atapin K., Solovyeva Y., 2020, *ApJ*, **893**, L28  
 Walton D. J., et al., 2021, *MNRAS*, **501**, 1002  
 Weng S.-S., Feng H., 2018, *ApJ*, **853**, 115  
 Wiktorowicz G., Sobolewska M., Lasota J., Belczynski K., 2017, in Ness J.-U., Migliari S., eds, *The X-ray Universe 2017*. p. 237



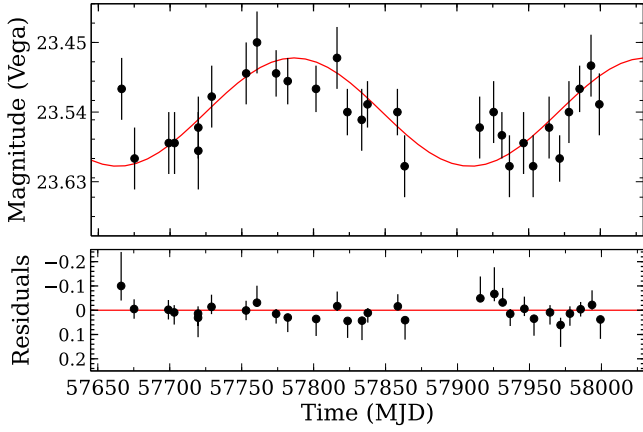


**Figure 7.** Sine curve fit and residuals for the light curve of counterpart A in the F606W observations. *HST* observations and sinusoidal fit represent filled black circles and solid red line, respectively. The residuals (data-model) are shown in the lower panel.

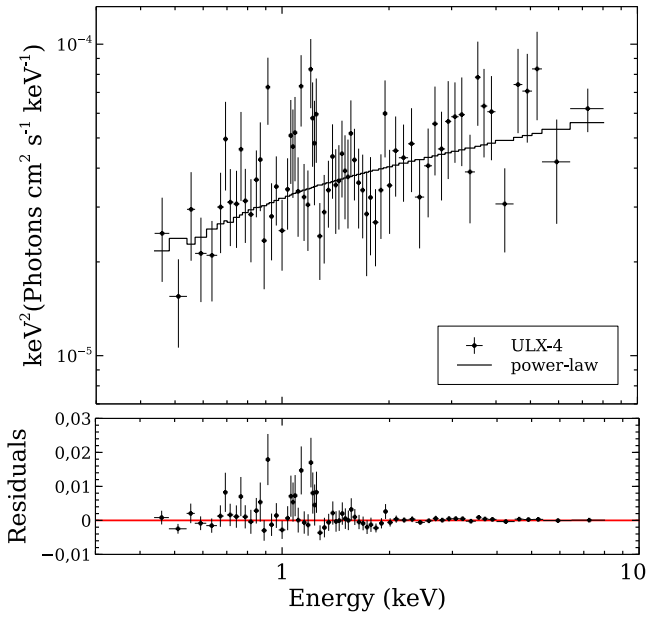


**Figure 8.** The upper panel shows the spectra unfolded through the *power-law* model from C12 data. The residuals (data-model) are shown in the lower panel.

Zampieri L., Impiombato D., Falomo R., Grisé F., Soria R., 2012, *MNRAS*, **419**, 1331  
 Zezas A., Fabbiano G., 2002, *ApJ*, **577**, 726  
 de Avellar M. G. B., Méndez M., Sanna A., Horvath J. E., 2013, *MNRAS*, **433**, 3453  
 van Haaften L. M., Maccarone T. J., Rhode K. L., Kundu A., Zepf S. E., 2019, *MNRAS*, **483**, 3566

This paper has been typeset from a  $\text{\LaTeX}$  file prepared by the author.

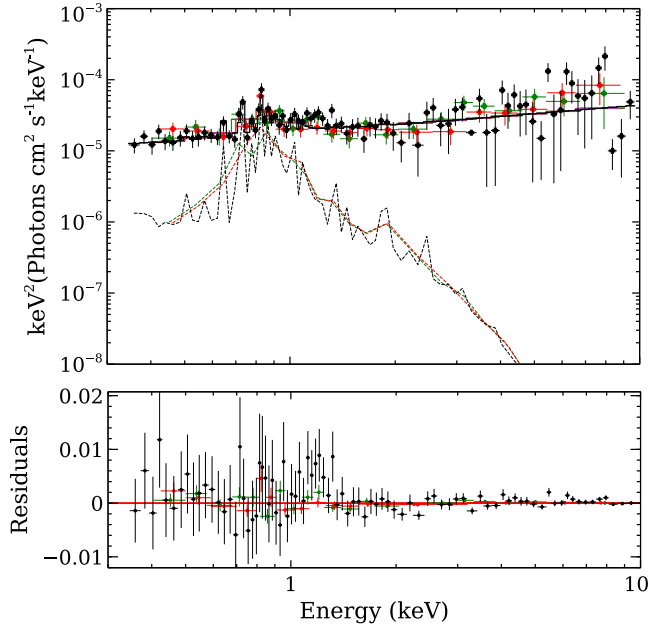


**Figure 9.** The upper panel shows the spectra unfolded through the *power-law+mekal* model from XM1 data. The residuals (data-model) are shown in the lower panel. The dashed black, red, and green lines represent the *mekal* model for pn, MOS-1, and MOS-2 data, respectively.

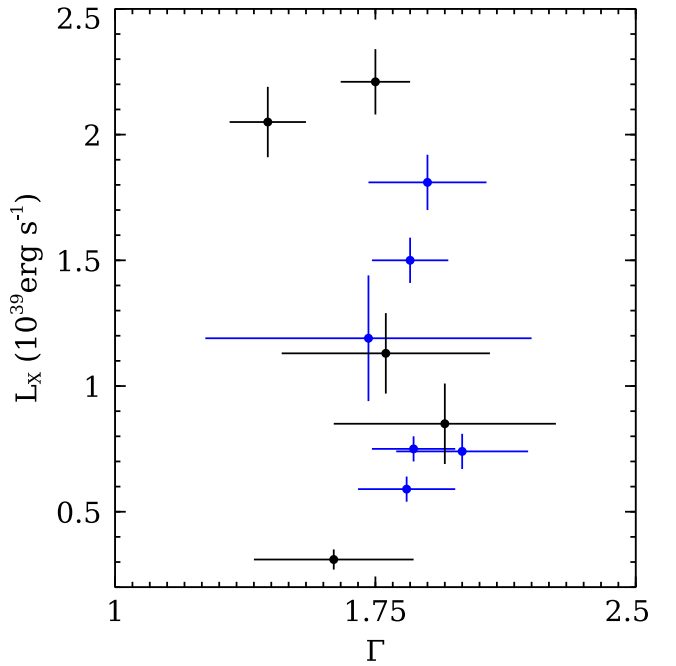


**Figure 10.**  $L_X$  derived from *power-law* model vs. photon index of  $\Gamma$  (see Table 2). Black and blue filled circles represent *Chandra* and *XMM-Newton* data, respectively.

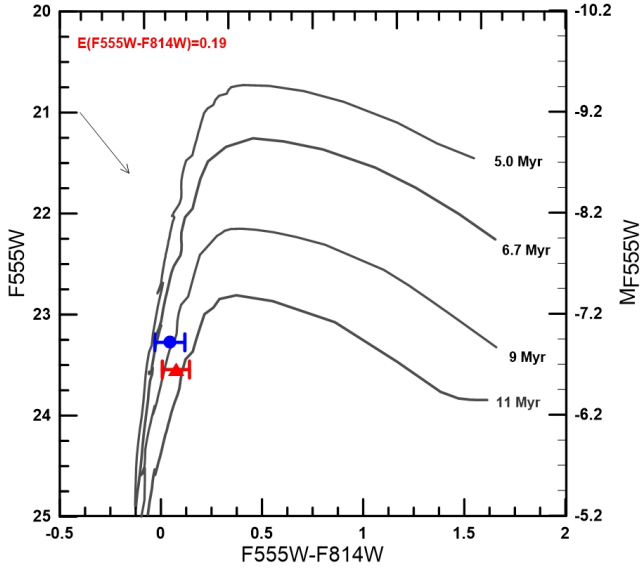


**Figure 11.** The *HST*/*ACS* Color-Magnitude Diagram (CMD) for optical counterparts of ULX-4. Padova isochrones of different ages are overplotted. The red triangle and blue circle represent counterparts A and B, respectively. These isochrones have been corrected for extinction  $A_V = 0.46$  mag and the reddening line was shown black arrow.

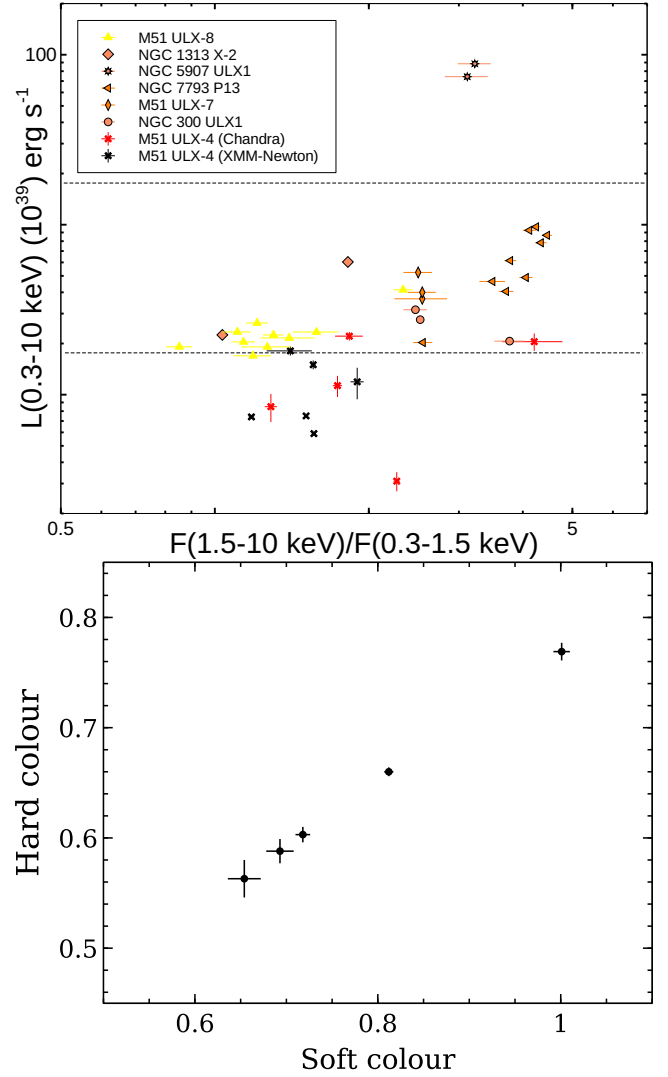


**Figure 12.** The upper panel, we imported the hardness-luminosity diagram of [Gürpide et al. \(2021\)](#) (their Figure 4) onto which we plotted the hardness-luminosity values extracted for ULX-4; *Chandra* and *XMM-Newton* data are denoted by red and black stars, respectively. Yellow triangles and in shades of orange represent NS ULX and pulsating ULXs, respectively. The dashed black lines show 10 and 100 times the Eddington limit for a NS. The hardness is determined as the ratio of the unabsorbed fluxes in the hard (1.5 – 10 keV) to soft (0.3 – 1.5 keV) bands. The lower panel: Colour-colour diagram for the *Chandra* data. Hard colour is defined as the ratio of the fluxes in the 5–8 and 2–5 keV while soft colour is defined as the ratio of the 1–2 and 0.3–1 keV.

**Table 6.** The dereddened Vega magnitudes of the counterpart A obtained from ACS/WFC F606W observations.

Date (MJD)	Magnitude (Vega)
57666.23008	23.51 $\pm$ 0.04
57675.23803	23.60 $\pm$ 0.04
57699.07316	23.58 $\pm$ 0.04
57703.11242	23.58 $\pm$ 0.04
57719.68467	23.59 $\pm$ 0.05
57719.68467	23.56 $\pm$ 0.04
57729.02204	23.52 $\pm$ 0.04
57753.05545	23.49 $\pm$ 0.04
57760.60783	23.45 $\pm$ 0.04
57773.93019	23.49 $\pm$ 0.03
57782.01584	23.50 $\pm$ 0.03
57801.73972	23.51 $\pm$ 0.03
57816.38990	23.47 $\pm$ 0.04
57823.60626	23.54 $\pm$ 0.03
57833.60502	23.55 $\pm$ 0.04
57837.64349	23.53 $\pm$ 0.03
57858.50069	23.54 $\pm$ 0.03
57863.53201	23.61 $\pm$ 0.04
57915.85382	23.56 $\pm$ 0.04
57925.58697	23.54 $\pm$ 0.04
57931.34880	23.57 $\pm$ 0.03
57936.61826	23.61 $\pm$ 0.04
57946.45948	23.58 $\pm$ 0.04
57953.14623	23.61 $\pm$ 0.04
57964.26810	23.56 $\pm$ 0.04
57971.61629	23.60 $\pm$ 0.03
57978.10350	23.54 $\pm$ 0.04
57985.54818	23.51 $\pm$ 0.03
57993.48529	23.48 $\pm$ 0.04
57999.30881	23.53 $\pm$ 0.04